Observed modulation of wintertime Western Arctic mixed-phase cloud properties by sea ice conditions, their long-term variabilities and trends

Pablo Saavedra Garfias[1,2] and Heike Kalesse-Los[1]

[1]Institute for Meteorology, Faculty of Physics and Earth System Sciences, Leipzig University, Leipzig, Germany.
[2]Leibniz Institute for Atmospheric Physics at the University of Rostock, Kühlungsborn, Germany.

Correspondence: P. Saavedra Garfias (pablo.saavedra@uni-leipzig.de)

Abstract. To assess the long-term interaction between sea ice conditions and Arctic mixed-phase cloud (MPC) properties, fourteen winter seasons of observations from the North Slope of Alaska are analysed. MPC properties are ~~set into context with~~ contextualized with respect to sea ice conditions by ~~determining the sea ice sectors which are most relevant to interact with~~ identifying the most relevant upstream sea ice sector influencing the observed clouds. A conical sector ~~of~~ with a 6° ~~and~~ azimuthal width and a 50 km radius~~of upstream sea ice concentration (SIC) is considered .~~, based on the ~~azimuth direction of the~~ direction of maximum water vapour transport (WVT) within the atmospheric boundary layer~~. The WVT height~~ , is considered. The height of the WVT is used as indicator of its interaction with the cloud, ~~allowing it to be classified~~ enabling classification as either cloud-coupled or decoupled. ~~The~~ MPC properties are further classified according to the presence of high or low pressure systems and analysed as a function of ~~SIC. Results highlight~~ sea ice concentration (SIC). Results indicate which MPC properties ~~significantly change~~ exhibit significant changes as SIC decreases. The long-term time series ~~evolution shows~~ reveal both positive and negative trends in MPC properties, depending on the WVT coupling status and the prevailing atmospheric pressure system. ~~The study finds statistically~~ Statistically significant positive trends ~~suggesting an increase of~~ are found, suggesting increases in sea ice-MPC coupled liquid water path (+35.0±0.9 $\mathrm{g\,m^{-2}\,decade^{-1}}$), cloud base height (+44.0±0.7 $\mathrm{m\,decade^{-1}}$) and cloud top temperature (+2.2±0.7 $\mathrm{K\,decade^{-1}}$) under low pressure weather systems. ~~It is also revealed that~~ Additionally, the evolution of MPC properties ~~presents cyclical characteristicsand it is hypothesized that those are~~ display cyclical characteristics, which are hypothesized to be in phase with climate oscillations like ENSO or PDO. Although the results support this hypothesis, ~~a direct causation is not trivial~~establishing a direct causal link remains non-trivial.

Copyright statement. TEXT

1 Introduction

Climate physics has long ~~ago established that increases in atmospheric concentrations of greenhouse gases~~ established that increasing atmospheric greenhouse gas concentrations warms the atmosphere (Arrhenius, 1897; Hegerl, 2022). Observations

in recent decades have suggested over recent decades indicate that the Arctic is warming two to four times faster than the whole Earth global average (Rantanen et al., 2022; Wendisch et al., 2023; Tan et al., 2023), a phenomenon known as Arctic amplification (AA) (Serreze and Francis, 2006; Serreze and Barry, 2011). Studies have shown that AA in climate models is related to the response to external forcingsClimate models attribute AA primary to external forcing, primarily the atmospheric lapse-rate feedback as well as sea ice related feedbacksand sea ice loss. However, the lack of full consensus on uncertainty in the magnitude of AA is attributed to the failure persist, largerly due to models' limited ability to simulate the sensitivity of Arctic sea ice loss to the rise of global temperature rising global temperatures (Notz and Community, 2020; Rantanen et al., 2022).

During Polar night, Arctic mixed-phase clouds have (MPC) exert a positive cloud radiative effect (CRE), which foster the warming of the surface beneath (Shupe and Intrieri, 2004; Cox et al., 2015). The CRE feedback mechanism contributes to AA and enhancing surface warming and contributing to sea ice decline . The magnitude of this forcing (Shupe and Intrieri, 2004; Cox et al., 201 . The strength of this feedback depends on micro- and macro-physical cloud properties (Shupe and Intrieri, 2004; Tan and Storelvmo, 2019). Extensive efforts are currently being performed to improve As a result, improving the understanding of the role MPCs MPC's role in a changing Arctic (Morrison et al., 2012; Korolev and Milbrandt, 2022; Tan et al., 2023) as well as to improve their representation in weather and climate models (Schemann and Ebell, 2020; Hofer et al., 2024; Tan et al., 2025) . Recently, Cesana et al. (2025), albeit –both in terms of their role in climate feedbacks and their representation in models– is a major research priority (Morrison et al., 2012; Korolev and Milbrandt, 2022; Tan et al., 2023; Schemann and Ebell, 2020; Hofer et al., 202 .

Recent studies highlight the importance of realistic cloud representation for simulating sea ice trend. Cesana et al. (2025) , though focused on Antarctica, found that prescribing winds wind fields in climate models improves the modeled variability simulation of sea ice and clouds variability compared to satellite observations. They further pointed out that a realistic representation of clouds emphasized that accurate cloud representation is crucial to capture the observed sea ice trends that climate models struggle to reproducetrends–challenge that current climate models still face. Large scale Pan-Arctic studies have highlighted contrasting differences between clouds located above sea ice or reveal contrasting cloud characteristics over sea ice versus open water: Palm et al. (2010) reported that areas with little or no sea ice are correlated with more cloudiness and a higher frequency higher cloudiness frequency and geometric thickness of low level clouds . They also over open ocean, while they found an increase of geometrically thicker clouds cloud geometrical thickness over open water. Li et al. (2020b) explained found that newly re-frozen sea ice areas can mitigate the development of low level clouds due to the low level cloud development due to imbalanced heat and moisture sourcesfluxes. Furthermore, sea ice concentration (SIC) changes can alter the thermodynamic phase distribution of wintertime MPC can be perturbed by sea ice concentration changes due to the through convective heat transfer over leads or and polynyas (Andreas and Cash, 1999). Papakonstantinou-Presvelou et al. (2022) found that Arctic low-level clouds contain more ice crystals in low-level clouds over sea ice than over open ocean, which is attributed to the amount and type of aerosols characteristic of each surfacewater, attributing this to surface-specific aerosol types. While sea ice leads have been are identified as main wintertime source sources of sea spray aerosols, there are limitations regarding the

quantification of amounts and drivers of sea spray emitted from leads their emission rates and drivers remain poorly quantified (Lapere et al., 2024).

Using synergistic atmospheric observations on-board the research vessel (RV) Polarstern during the year-long Multidisciplinary drifting Observatory for the Study of Arctic Climate MOSAiC expedition (Shupe et al., 2022) from (2019 to – 2020, Saavedra Garfias et al. (2023) have proposed a mechanism to physically link the) (Shupe et al., 2022), Saavedra Garfias et al. (2023) proposed a physical mechanism linking local sea ice states in the vicinity of RV Polarstern with the MPC observed above it. By exploiting a novel to MPC properties above the ship. By leveraging a high-quality, high-resolutionsatellite based , satellite-derived sea ice lead fraction estimation, which was specifically derived product specifically developed for MOSAiC along the RV Polarstern drifting path (von Albedyll et al., 2024), Saavedra Garfias et al. (2023) found that some properties of MPC when MPC properties –particularly liquid water path (LWP)– are positively correlated with upstream lead fraction when clouds are coupled to the sea ice leads via the water vapour transport , are correlated to the upstream sea ice lead fraction. Among those properties the most remarkable is the liquid water path (LWP)which is positively correlated with the amount of sea ice lead fraction. Conversely, the (WVT). In contrast, ice water path (IWP) was not found to be correlated with sea ice leadsshowed no significant correlation with lead fraction.

The majority of previous studies relating MPC properties Most prior studies linking MPC and sea ice state either consider large spatial scales or short term observations. This hinders the evaluation of those findings within a climate modelling context. Although models are able to capture several rely on either large-scale or short-term observations, limiting their utility for climate model evaluation. While models can capture some aspects of MPCrealistically, they e.g. struggle , they often fail to accurately represent thermodynamic phase and ice/liquid water path (Schemann and Ebell, 2020; Pithan et al., 2014). At the same timeMoreover, current climate models do not sufficiently take into account inadequately simulate how MPC properties change in evolve under a warming climate (Cesana et al., 2025; Nakanishi and Michibata, 2025). Thus, long-termcloud , high-quality observations are paramount to evaluate climate modelsfor climate model validation. Manaster et al. (2017) analysed over 20 years of multi-satellite products data to estimate global liquid water path (LWP) trends over oceansand evaluated them against , comparing them with CMIP5 models. Although they did not include the their study excluded polar regions, their results are one of the few references for the long-term rate of change of LWP, with positive . They reported a positive LWP trends of about 1-2 $\mathrm{g\,m^{-2}\,dec^{-1}}$ reported for in the Southern Ocean and the North Pacific. They also found that discrepancies between observations and CMIP5 models cannot be explained by removing sources of found that removing inter-annual variabilitylike , e.g. El Niño Southern Oscilation (ENSO), concluding that did not resolve model-observation discrepancies, suggesting ENSO is not a major parameter to affect the LWP trends. They did however not discard the possibility that other modes of variability could have a larger impact on LWP trends, the dominant driver–though other modes (e.g.the Pacific Decadal Oscillation(PDO) , Pacific Decanal Oscillation, PDO) may play a larger role.

This brings up two questions: Firstly, can the MOSAiC -based findings of Saavedra Garfias et al. (2023)obtained for one winter of observations of MPC properties linked to sea ice state in the Central Arctic be confirmed –derived from a single winter in the central Arctic–be confirmed using for long-term observations in the Western Arctic?. Secondly, are Arctic MPC properties correlated with modulated by climate variability modes that are not evident from not evident in short-term studies?

Answering these questions ~~will advance our knowledge on how~~ advances our understanding of ocean-sea ice-atmosphere interaction and ~~feedback processes modulate~~ their feedbacks on Arctic cloud properties, ~~which in turn provides valuable information for better representation of MPC~~ providing critical insights for improving MPC representation in weather and climate models. ~~For thispurpose~~To address this, the present study applies the methodology ~~developed by Saavedra Garfias et al. (2023) to long-term~~ of Saavedra Garfias et al. (2023) to 14 winter seasons (2011 to 2024) of wintertime MPC observations at the ARM North Slope of Alaska (NSA) site in the Western Arctic~~ranging from 2011 to 2024~~ .

The manuscript is ~~organized~~ structured as follows: ~~in~~ Sec. 2 ~~we present details about~~ details the measurement site, instrumentation, data processing, and analysis methods~~adopted for the present study. Results are presented in~~ . Sec. 3 ~~. Specifically, the new findings regarding~~ presents results, including the modulation of MPC properties by sea ice conditions for the entire 14 years ~~as well as the year-to-year-variability and trends are reported in~~ (Sec. 3.1~~and~~), the year-to-year-variability (Sec. 3.2~~-~~), and trends (Sec. 3.2.3), respectively. ~~These results are further discussed in Sec~~Section. 4 ~~by highlighting how the present work corroborates or contradicts previous results obtained by the same method from the MOSAiC expedition in the Central Arctic. Finally, Sec. 4 summarizes the implications of our results . Additionally,~~ discusses these findings in the context of MOSAiC results and their implications. Supplementary materials include detailed descriptions of data availability,, statistical methods, climatological analysis, nomenclature description, and ancillary results~~can be found in the appendixes and in the supplementary document, respectively~~.

2 Data and Methodology

The U.S. Department of Energy's Atmospheric Radiation Measurement (ARM) program ~~of the US Department of Energy~~ (www.arm.gov) provides long-term~~comprehensive~~ , high-quality observations for clouds and radiation at multiple ~~locations~~ sites around the world. ~~In particular for Arctic studies~~ For Arctic reseach, one of the few sources of quasi ~~uninterrupted~~ continuous, long-term observations is the ARM ~~'s~~ North Slope of Alaska (NSA) ~~, observational sitelocated at a latitude~~ site, located in Utqiaġvik, Alaska (71.323° North and ~~longitude of~~ 156.609° West~~, in Utqiaġvik, Alaska~~), in the Western Arctic (Fig. 1). In ~~the present~~ this study, we ~~utilize cloud observations of fourteen winter seasons ranging from~~ use 14 winter seasons (November 1^{st} to April 30^{th} ~~from the NSA site to characterize MPC and investigate the change of their properties governed by different~~) of NSA site observations to characterize mixed-phase clouds (MPC) and investigate how their properties are influenced by upstream sea ice conditions. ~~For that purpose,~~ To this end, we adapt and apply the methodology developed by Saavedra Garfias et al. (2023)~~(~~, hereafter referred to PSG23~~) is adapted and applied to the suite of instrumentation available at the NSA site~~, to the ARM NSA site instrument suite, as described in the following section.

2.1 ARM atmospheric remote sensing instrumentation

The primary ~~set of remote sensing instruments from which data was~~ instruments used to characterize MPC are the ARM Ka-band zenith-pointing cloud radar (KAZR), the Vaisala CL31 cloud ~~lidar (ceilometer)~~ ceilometer (lidar), and a dual-frequency microwave radiometer (MWR). Moreover, ~~the~~ atmospheric boundary layer (ABL) parameters and thermodynamic

Table 1. Specifications of instrumentation, data products and their references used for this study. VAP refers to ARM's Value Added Product.

NSA site observatory					
Instrument/VAP	Full name	Variables/Producs **	Resolution		Reference
			time	range	
MWR RET	passive microwave radiometer	LWP, IWV	1 s	-	Zhang (2024)
MWR LOS*	passive microwave radiometer	LWP, IWV	1 s	-	Cadeddu et al. (2024)
KAZR ARSCL	Ka-band cloud radar	Ze, V_D, S_w, LDR	3 s	30 m	Johnson et al. (2024)
KAZR CORRGE*	Ka-band cloud radar	Ze, V_D, S_w, LDR	3 s	30 m	Toto and Giangrande (2024)
CEIL10m	Ceilometer 10m	β, CBH	16 s	10 m	Zhang et al. (2024)
INTERPSONDE	Interpolated Radiosonde	T, P, q_v, $\boldsymbol{V}$	1 min	20 m	Jensen et al. (2024)
FLUXRAD	Down/upwelling longwave radiation	T_{skin}, Ri_b, PBLH	1 min	-	Riihimaki et al. (2024)
GND_IRT*	Ground Infrared Thermometer	T_{skin}, Ri_b, PBLH	1 min	-	Shi et al. (2024)
Space-borne sensor					
AMSR2	region Chukchi-Beaufort	n3125 SIC	1 day	3.2 km	Melsheimer and Spreen (2019)
AMSR2*	region North West Passage	n3125 SIC	1 day	3.2 km	Melsheimer and Spreen (2019)
SSMIS17*	region North West Passage	n3125 SIC	1 day	3.2 km	Melsheimer and Spreen (2019)
Ancillary data					
ECMWF	Cloudnet Numerical Prediction	all	1 hour	–	O'Connor (2025)
–	Arctic Oscillation index	AO	1 day	-	NOAA AO
–	El Niño Southern Oscillation	ENSO	1 week	-	JPL ENSO
–	Pacific Decadal Oscillation	PDO	1 week	-	JPL PDO

* used as alternative to reduce data gaps. **See appendix E for full definition of acronyms.

states are estimated from ~~the synergy of ground~~ synergy between the ground-based infrared radiometer (GND_IRT) and ~~radiosondes launched regularly~~ regular radiosondes launched from the NSA site. Table 1 summarizes the instruments, relevant data products, ~~their~~ spatial and temporal resolutions, and ~~a list of corresponding referencesthat are utilized in the present study~~their corresponding references. A detailed ~~availability time-line for the total period of study is shown~~ timeline of data over the study period is provided in Fig. S14 ~~of~~ (supplementary material S4). Additionally, ~~observations of sea ice conditions from space-borne sensors are needed~~ satellite-derived sea ice observations are required to complement the ~~set of required~~ atmospheric data for the application of the PSG23 method. The processing and merging of sea ice data with the atmospheric observations ~~is~~ are explained in Sec. 2.3.

2.2 Characterization of the cloudy atmosphere

Figure 2 ~~shows an example for~~ illustrate the synergy of ~~observations by the KAZRcloud radar, the ceilometerand the MWR for the case of~~ KAZR, ceilometer, and MWR observations for a case on January 19th, 2019. These ~~sets of observations together with the atmospheric thermodynamic information obtained either~~ data, combined with thermodynamic profiles from

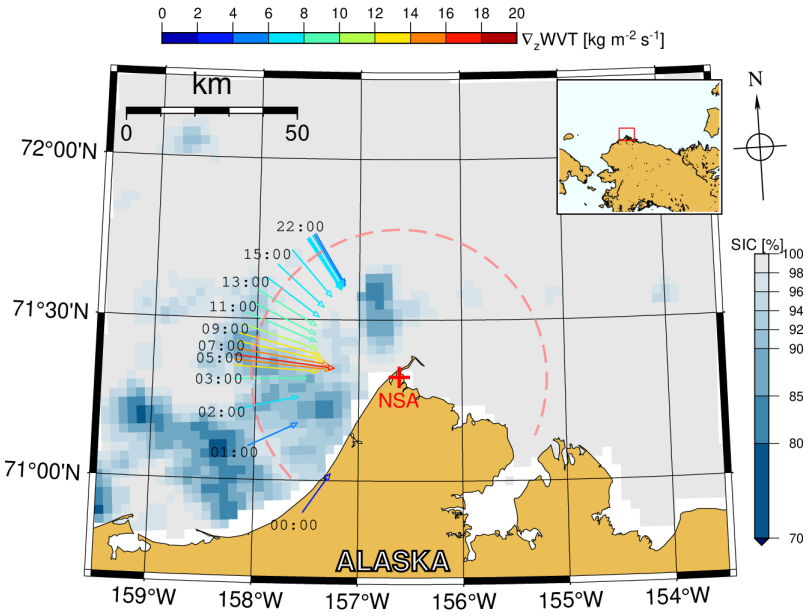


Figure 1. ARM's North Slope of Alaska NSA site (red cross: 71.23° North, 156.61° West) in Utqiaġvik, Alaska (top right inlet). Right-bottom colour scale indicates the AMSR2 sea ice concentration (SIC) from January 19th, 2019. Red-dashed 50 km semi-circle marks the sub-sector around NSA site considered in this study. The coloured radial arrows depict the direction of ∇_zWVT at selected times throughout the day for visualization purposes (see Sec. 2.4) as observed above NSA site.

the ECMWF numerical weather model (O'Connor, 2025) or radiosonde ~~profiles are~~ soundings, form the basis for ~~the algorithm that classifies the~~ classifying cloud thermodynamic phase and hydrometeor type~~of the cloudy atmosphere~~. The retrieval algorithm ~~utilized~~ used in this study is the state-of-the-art Cloudnet target classification algorithm (Illingworth et al., 2007; Tukiainen et al., 2020) version CloudnetPy 1.68.1 ~~shown in~~ (Fig. 2 (d)~~. By default the~~). Since ARM data are not ~~supported by CloudnetPy, therefore the data from the instrumentation listed in~~ natively compatible with CloudnetPy, the raw instrumentation data (Table 1~~had to be adapted to be a compliant input (?). In addition to the standard Cloudnet classification products, other atmospheric and cloud properties are calculated, namely~~) were pre-processed and adapted to meet input requirements (Saavedra Garfias, 2022) Beyond standard Cloudnet products, additional cloud and atmospheric properties are computed: atmospheric boundary layer height, cloud base and top heights, and cloud top temperature for each cloud layer. Readers are referred to PSG23 for details.

Accurate characterization of ~~Arctic~~ low-level Arctic stratus clouds is compromised when the ~~base of a~~ liquid-containing cloud ~~layer is detected by the lidar at altitudes~~ base lies below the radar's lowest detection range. As ~~explained in Griesche et al. (2020) , the distribution of the LWP depends on whether a higher liquid-containing cloud layer was observed or not. When the low-level stratus cloud attenuates~~ noted by Griesche et al. (2020), if the lidar signal ~~below the radar lowest detection range no~~ is attenuated by a low-level liquid layer and no higher liquid layer is ~~identified by Cloudnet at all and~~ detected, Cloudnet classifies the entire profile ~~is classified as ice. In that case, the~~ as ice, leading a complete omission of LWP from the ~~microwave~~

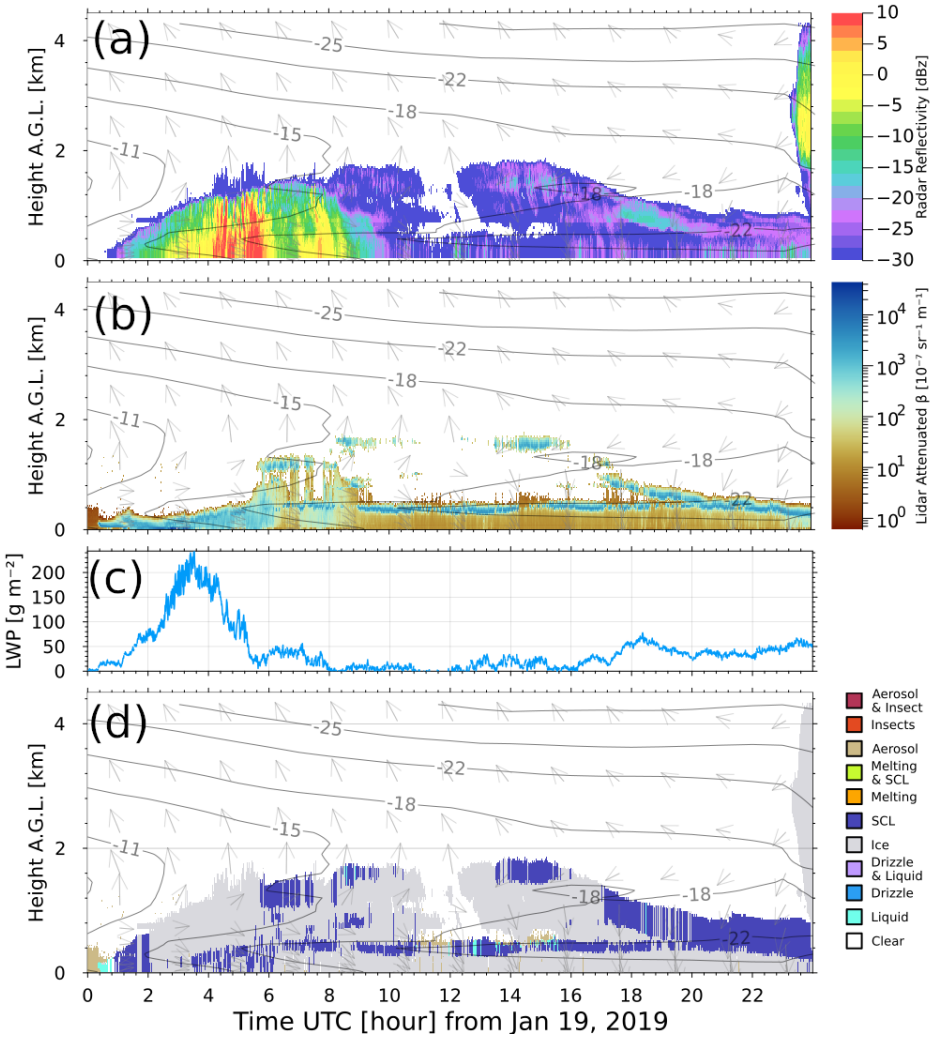


Figure 2. Synergistic ground-based remote sensing observations at NSA on January 19, 2019. Ka-band cloud radar (KAZR) reflectivity factor (a), ceilometer Vaisala CL31 attenuated backscattering coefficient β (b), dual-frequency MWR liquid water path (c), Cloudnet target classification (d) with supercooled liquid (SCL) in blue. Panels (a), (b) and (d) include profiles of the ECMWF numerical weather prediction model horizontal wind vector (arrows) and temperature (~~iso-therms~~isotherms).

~~radiometer is simply ignored (as in~~ MWR (e.g., Fig. 2 2-3:30 UTC). ~~If an other liquid cloud~~ However, if a higher liquid layer is present~~higher up, Cloudnet distributes the LWP measured by the microwave radiometer to that layer. Griesche et al. (2020, 2024) reported that~~ , the MWR LWP is distributed accordingly. Griesche et al. (2020, 2024) report that for the MOSAiC expedition such low-level stratus ~~cloud cases occur more than~~ cases occur in over 25% of ~~the observation time. Also, they found for the MOSAiC expedition that low-level stratus are more frequently observed during~~ observation time, with higher frequency in summer than winter. ~~For the NSA site~~At the NSA site, the lidar can detect liquid ~~at altitudes as low as~~ clouds down to 10 m ~~whereas~~

the radar altitude, whereas the KAZR has a lowest detection range of 160/100 m for the KAZR's ARSCL/CORRGEproducts m (ARSCL) and 100 m (CORRGE), respectively (detail in references see references in Table 1). The present study has found finds that low-level clouds below radar detection range of the radar's detection threshold (160 m (for ARSCL, 100 m) comprises about for CORRGE) account for approximately 26% (and 22.5%) of data. To overcome of observations, respectively. To mitigate this limitation, in the present study the database is adjusted by the dataset is adjusted via a flat extrapolation of KAZR's radar reflectivity applied radar reflectivity down to the lidarliquid layer detection , before the cloud characterizationis performed's lowest liquid detection altitude (10 m) prior to cloud characterization.

Furthermore, one of the main short-comings A key limitation of the Cloudnet target classification is that cloud liquid detection is solely based on a algorithm is its reliance on valid lidar signal . In for liquid cloud detection. As shown in Fig. 2 , at (2-4 UTC,), complete attenuation of the lidar signal is fully attenuated by liquid within the lowest range gates of the ceilometer. Thus, higher supercooled liquid-layers remain undetected and all pixels without valid lidar signal are classified by Cloudnet by low-level liquid layers results in the misclassification of higher supercooled liquid layer as ice. More sophisticated Consequently, liquid water content is underestimated, and ice-only clouds are overestimated. More advanced cloud radar Doppler spectra-based tools such as introduced in –such as those introduced by Kalesse-Los et al. (2022) and Schimmel et al. (2022)would be able to – can detect liquid beyond full lidar signal attenuation. However, , but their application would require novel training extensive retraining on the NSA dataset and extensive computing processing time which is significant computation resources, which are beyond the scope of this study. As a takeaway, the amount of MPC detected by Cloudnet used here has result, the Cloudnet derived MPC dataset used here exhibits a low bias whereas in liquid-phase detection, while ice-only clouds are overestimated.

The Cloudnet processing chain , applied –applied to 14 years of NSA data, is the backbone for creation of a combined data– forms the basis for a merged dataset of macro- and micro-physical cloud propertiesmerged , combined with sea ice conditions (as explained in see Sec. 2.3)similarly to Saavedra Garfias and Kalesse-Los (2023). This approach follows Saavedra Garfias and Kalesse-Lo , where MPC are considered when retained only when both LWP and IWP , exceed 5 $\mathrm{g\,m^{-2}}$ in a single cloud layer, are equal or greater than 5 $\mathrm{g\,m^{-2}}$ to avoid introducing layer, minimizing uncertainties from retrieval algorithms due to instrument minimum detectable capabilitiesdetection thresholds.

2.3 Characterization of sea ice conditions around NSA site

The PSG23 method utilized originally used high-resolution (700 m) sea ice lead fraction (LF) at a high spatial resolution of 700 m. LF was derived from sea ice divergence imaging from Synthetic Aperture Radar satellite (SAR) satellite imagery specifically developed for the MOSAiC expedition (von Albedyll et al., 2024). That quality level of LF product does not exist However, such high-resolution LF products are not available for the multi-year observations at the NSA site, which is a major difference for the application of the PSG23 method in the present studyNSA site observations. Instead, we use sea ice concentration (SIC) is obtained from the University of Bremenpublic repository 's publicly available satellite-based Arctic sea ice products (www.seaice.uni-bremen.de, e.g. (Spreen et al., 2008; Melsheimer and Spreen, 2019)) to characterize the ocean conditions surrounding NSA site. SIC the NSA site. The SIC product is retrieved from brightness temperatures observations

measured by the Advanced Microwave Scanning Radiometer-2 (AMSR2) ~~sensor which has been in operation~~ onboard the Global Change Observation Mission 1st GCOM-W1 satellite since autumn 2012. ~~The product retrieved is the~~ AMSR2 sea ice (ASI) ~~concentration at a Polar stereographic grid size of~~ provides daily SIC at 3.124 km ~~and daily temporal resolution (Spreen et al., 2008)~~ polar stereographic grid resolution (see "Space-borne sensor" in Table 1) ~~. The University of Bremen~~ provides ASI products for the whole Arctic as well as selected regions of interest. The present studyuses the regions identified as (Spreen et al., 2008). For this study, we use the "Chukchi-Beaufort" region (Fig. 1)~~which is centered close to the NSA site longitude and covers the western- and eastern-part~~ , centred at the NSA site and covering the western and eastern part of the Chukchi and Beaufort ~~seas, respectively. Furthermore, from the whole "Chukchi-Beaufort" sector only a small subset of grid cells are considered to be relevant for the PSG23 method, i.e.~~ Seas. To identify the most relevant sea ice conditions ~~that are most likely to interact with the atmospheric boundary layer clouds at the NSA site (Sec. 2.2). The sub-sector considered for the present study is a semi-circle centered at NSA site with~~ for cloud interaction, we defined a 50 km radius ~~and limited from~~ semi-circular sector centred at NSA site (red dashed line in Fig. 1) spanning azimuths from -125° to 110~~° azimuth (red-dashed delimited semi-circle sector in Fig.1). Because we are exclusively interested in the sea ice-cloud interaction, the complementary semi-circular sector covering the land is dismissed.This means MPC~~ °. This sector excludes the landward side (i.e. southerly inflow), ensuring that only clouds, with CTH $\leq$ 3 km~~being advected from the land to the NSA site are excluded from this study, which corresponds to~~ , advected from open or ice-covered ocean areas are considered. This exclusion removes ~8.1% of the data, corresponding to clouds originating from land.

~~Mean~~ The mean and standard deviation of ~~the~~ SIC are used~~here. It is assumed that SIC follows~~ . SIC is assumed to follow a truncated normal distribution with lower and upper truncation limits of 0% and 100%, respectively. The PSG23 method ~~considers only a~~ further restricts analysis to a $\pm 3°$ conical sector extending from the NSA site outwards up to 50 km ~~with angular width of $\pm 3°$. The azimuth of the conical sector is governed by the horizontal wind vector~~ and aligned with the upwind direction $\boldsymbol{v}_w$ ~~at a height where~~ of maximum vertical gradient of water vapour transport (∇_zWVT ~~is at maximum (details~~), as described in Sec. 2.4~~). Subsequently, the~~ . The mean sea ice concentration within the conical sector is denoted by SIC, whereas the mean sea ice concentration ~~for the entire~~ over the full 50 km semi-circular sector ~~(red-dashed in Fig. 1) is denoted by~~ is denoted as $\mathrm{SIC}_\odot$ (Fig. 3). ~~Details about the yearly difference between the statistics given by the entire circle around NSA site $\mathrm{SIC}_\odot$ and the conical sector SIC aligned to $\boldsymbol{v}_w$,~~ The annual differences between these two metrics are shown in Fig. S1 ~~in supplement~~ (Supplementary material S1.1.

Between 2011 and ~~2024~~2025, the Chuckchi-Beafort ~~seas area experienced~~ region experienced several winters with extraordinary low ~~sea ice concentration ($\mathrm{SIC}_\odot \lesssim$~~SIC ($\lesssim$50% in Fig. 3 and Fig. S1), ~~e.g.~~ including 2012/13, 2016/17, 2017/18, 2019/20, 2023/24, and 2024/25. These ~~anomalously low sea ice winters can be partially related~~ anomalies are likely linked to climatological variability and/or ~~forcing from low latitudes~~low latitude forcing. For example, ~~using observations and model simulations for the Barents-Kara seas area Zhang et al. (2023) revealed that the decrease of sea ice area is correlated with an increase of the~~ Zhang et al. (2023) found that increased frequency of atmospheric rivers ~~reaching the Arctic in winter . They~~ in winter correlates with reduced sea ice in the Barents-Kara seas. Atmospheric rivers prevent the sea ice recovering from summer melt and from growing to the climatologically expected sea ice coverage in winter. For the Chukchi-Beaufort ~~seas, and for the period~~

region (2011 to 2020~~, the frequency of atmospheric rivers~~), atmospheric river frequency (averaged over November to April) has maximum values of 5.3% in 2018/19, ~~an intermediate value of~~ with intermediate value (2.6%) in 2013/14, 2014/15, and 2019/20, ~~plus~~ and a minimum value of 0.2% in 2015/16 (personal communication with Zhang et al. (2023) lead author). The wintertime 2018-2019~~with~~ , despite moderate atmospheric river activity, saw a less frequent but still noticeable $SIC_{\odot} \lesssim 50\%$ ~~in~~ (Fig. S1~~, can be attributed to the~~), likely due to anomalous warm ocean ~~water as response to the southerly winds associated with~~ waters driven by southerly winds and episodic atmospheric blocking over the Bering Sea in September 2018 ~~which was directly~~ directly observed by the R/V Mirai Arctic Expedition in November 2018 (Kodaira et al., 2020).

2.4 ~~Coupling sea~~ Sea ice - atmosphere coupling via water vapour transport

Winter sea ice ~~open areas (e.g. leads or polynyas) are effective local~~ leads and polynyas act as localized sources of heat and moisture released to the atmosphere. ~~Because of~~ Through convection and advection, ~~plumes of heat and moisture~~ these plumes can be transported ~~afar from the location where the sea ice lead or polynya occurs and interact with the clouds. This interaction is needed to be established in order to relate the sea ice concentration and the cloud properties. This is performed by applying~~ downstream and influence cloud properties. To establish a physical link between sea ice and clouds, we apply the PSG23 methodology~~. Whether a cloud is influenced by the sea ice-ocean system or not is determined by taking advantage of~~ , using the water vapour transport (WVT) as a physical mechanism to link, akind a conveyor belt, the upstream sea ice conditions and the measured cloud properties above the ~~NSA site. Specifically, the~~ NSA site (Saavedra Garfias et al., 2023). WVT ~~, which is estimated~~ is derived from radiosonde profiles ~~, was proposed by Saavedra Garfias et al. (2023) to physically link, akin a conveyor belt, the heat and moisture released by sea ice openings and transport them downstream to interact with the cloud over an observatory location and perturb its properties.~~

~~The WVT normally~~ and represents the magnitude and direction of water vapour flux and consists of several bands of different magnitudes along the vertical profile. ~~In order to determine which bands are the most relevant to be interacting with a cloud, the~~

The PSG23 method ~~limits the WVT vertical profile to~~ identifies the most relevant WVT layer using its vertical profile gradient ($\nabla_z \mathtt{WVT}$ ~~[kg m^{-2} s^{-1}]~~) within the planetary boundary layer height (PBLH)~~, which is estimated by~~ . The PBLH is constrained when the bulk Richardson number ~~when it is~~ $Ri_b \approx 1$. The ~~PSG23 method determines the most relevant WVT band (if several are present) by means of its vertical gradient (~~vertical gradient of $\nabla_z \mathtt{WVT}$ ~~[kg m^{-2} s^{-1}])~~ is calculated using Eq. 1 ~~. Please note that (~~a detailed derivation is given in Saavedra Garfias et al. (2023)~~. In summary, to classify cases where the WVT is coupled or decoupled to the cloud, the cumulative variance of virtual potential temperature θ_v is analysed from the cloud base/top height downwards/upwards to bottom/top altitudes where the variance exceeds a certain threshold. These altitudes are then assigned as cloud mixing layer limits. When the vertical profile has a local maximum at an altitude within the cloud mixing layer limits, that cloud is assigned to be coupled (denoted as "co") to the sea ice-WVT system, otherwise is considered to be decoupled (denoted as "de"). is calculated as~~

).

$$\nabla_z \mathtt{WVT} = -\frac{10^2}{g} \left| q_v \cdot \boldsymbol{v}_w \right| \frac{dP}{dz} \tag{1}$$

where ∇_z indicates the vertical gradient, g is the constant of gravity, with the specific humidity q_v [g kg^{-1}], horizontal wind speed $\boldsymbol{v}_w$ [m s^{-1}], and air pressure P [Pa] at altitudes z [m].

~~From all ASI grid cells within the 50 km semi-circle centered at NSA site, only SIC cells are considered that are located within the conical sector of~~ A cloud is classified as coupled (co) to the sea ice-WVT system if $\nabla_z \mathtt{WVT}$ has a local maximum within the cloud mixing layer –defined by the cumulative variance of virtual potential temperature θ_v from cloud base/top height downwards/upwards until a threshold is exceeded. Otherwise, the cloud is classified as decoupled (de).

Within the ASI grid cells a conical sector ($\pm 3°$ ~~around~~) is aligned with the upwind direction ~~. An example is shown in~~ at the altitude of maximum $\nabla_z \mathtt{WVT}$ (e.g., Fig. 1 where the radial arrows depict the direction of $\nabla_z \mathtt{WVT}$ ~~. Arrows are color-coded by the maximum~~ and their colour the magnitude). Only SIC values within this sector are used for analysis. At a given time the azimuth of the conical sector is governed by the upwind direction obtained from the altitude where $\nabla_z \mathtt{WVT}$ reaches its maximum. ~~In the following, the statistics are based uniquely on sea ice concentration present within the ± 3conical sector. Situations with winds coming from the land (i.e. Southerly~~ Southerly winds (landward flow) are ~~not considered in the analyzed dataset~~excluded. Figure S1 ~~stresses the fact that the~~ highlight a critical distinction: sea ice conditions ~~around NSA site are of completely different statistically nature than the sea ice conditions within the ± 3conical sectorthat interacts with the clouds above NSA site. Therefore, relating cloud characteristics observed from satellite or in-situ observations with a large area of sea ice can~~ in the full semi-circular sector differ significantly from those in the upwind conical sector. Thus, using large-scale SIC to infer cloud properties may lead to ill-posed correlations since not all sea ice conditions play a relevant role to explain observed cloud properties (e.g. Palm et al. (2010); Li et al. (2020a, b)).

2.5 NSA site atmospheric pressure systems and climatology

The NSA site climatology is ~~characterized~~ influenced by the persistent ~~influence of~~ cyclonic activity in the north-western Pacific Ocean and ~~anticyclones in~~ anticyclonic systems over the Beaufort/Chukchi seas (Serreze et al., 1993; Serreze and Barry, 2014). ~~Thus the atmospheric surface pressure is a useful indicator of events characterized by synoptically~~ Surface pressure serves as a proxy for synoptic-scale high (H-) or low (L-) pressure systems over NSA site (Fig. 3). Atmospheric air temperature and pressure are closely related to stability or instability in the atmosphere which strongly influences the formation of clouds. ~~The classification of local pressure system at any given time and base on measured local pressure and temperature is estimated~~ Local pressure systems are classified by the following steps: i) a reference virtual isobaric surface P_0 is assumed to separate the H- or L-pressure observations, ii) from the measured surface pressure and temperature, the relative height of the virtual isobar P_0 is determined. The relative height of P_0 is expressed in terms of geopotential height difference derived from the equation of state (Rogers and Yau, 1991):

$$\Delta Z = \frac{R\overline{T}}{g_0} \log\left(\frac{P_0}{P}\right) \tag{2}$$

where R is the specific gas constant 287.05 $\mathrm{J\,kg^{-1}\,K^{-1}}$, g_0 the acceleration of gravity at the surface 9.81 $\mathrm{m\,s^{-2}}$, $\overline{T}$ the mean temperature within the layer [K], P_0 the reference isobar surface (in this case the mean sea level pressure of 101.32 kPa), and P is the measured local surface pressure [kPa] at a given time. ΔZ ~~takes negative values for observations with a H-pressure~~ is negative for H-pressure systems (i.e. P>P_0), ~~conversely ΔZ is~~ and positive for L-pressure (i.e. P<P_0). ~~The~~ $\overline{T}$ is assumed to be the measured 2 m air temperature, and its effect is to adjust the magnitude of ΔZ when P ~~considerable departures~~ departures considerably from the reference P_0. ~~Within the analysed winters from~~

From 2011 to 2024 , surface pressures ~~measured at NSA are~~ at NSA were slightly biased towards H-pressure ~~with a medianof~~ (median: 101.69 kPa; and Inter-Quantile Region (IQR)~~of~~ : 100.95 ~~to~~ – 102.50 kPa~~. H-pressure systems were observed slightly more frequently (~~), with H-pressure systems occurring 56.3% of the time ~~) than L-pressure systems (~~and L-pressure systems 43.7% of the time~~)~~. The distribution of ΔZ ~~reveals an ample difference when sorted by the corresponding cloud observations' coupled or decoupled classification.~~ differs significantly between coupled and decoupled cases: Coupled: median ΔZ ~~for coupled caseshave a median of =~~ -9.45 m (IQR: -65.05 m ~~,~~ to 44.72 m)~~. In contrast decoupled cases have a median of~~ ; Decoupled: median -30.98 m (IQR: -86.95 m ~~,~~ to 18.74 m). ~~Accordingly,~~ This indicates that H-pressure systems favour ~~the formation of decoupled clouds. It is important to note~~ decoupled cloud formation. Note that ΔZ ~~is meant to be a representation of the local pressure at NSA site and cannot be taken as a substitute to synoptic pressure systems for the Western Arctic found in~~ reflects local conditions and does not replace synoptic-scale pressure systems from Western Arctic weather maps.

3 Results~~and discussion~~

NSA site wintertime (November 1^{st} to April 30^{th}) observations from 2011 to 2024 were analysed in accordance with the methodology outlined in the previous sections. ~~The results~~ Results are presented after ~~the~~ observations from the instruments listed in Table 1 were resampled to a common ~~1 minute~~ 1-minute time resolution and clustered ~~between~~ by high (ΔZ<0) and low (($\Delta Z \geq$0)) pressure weather systems~~and~~ , as well as by coupled (co), and decoupled (de) status. ~~Statistics of wintertime~~ Wintertime cloud properties are reported ~~based on~~ using two approaches: as a function of SIC~~as in~~ , following Saavedra Garfias et al. (2023) (Sec. 3.1), and as time series ~~along~~ over the 14 years (Sec. 3.2). ~~The results are presented as descriptive statistics by the distributions~~ Descriptive statistics are presented using the median ($\mu_{½}$) and ~~distributions variability~~ variability quantified by the median absolute deviation (MAD) defined ~~by~~ as $\sigma_{\mathrm{mad}} = \pm median(|X_i - \mu_{½}|)$. ~~Other statistical distribution descriptors have been used, for example~~ Additional statistical descriptors include the geometric mean (μ_g), the 25^{th}, and 75^{th} percentiles~~,~~ ~~however, if not explicitly noted otherwise , the following results are referring to~~ . Unless otherwise specified, results are reported as $\mu_{½} \pm \sigma_{\mathrm{mad}}$.

3.1 Modulation of MPC properties as a function of SIC, coupling status, and pressure system

For the considered time period the cloud, frequency of occurrence (FoO) were analysed. The total cloud FoO (Fig. 4, left bars) ~~shows a roughly constant FoO at about~~ remains approximately constant at ~75% throughout the ~~wintertime~~winter, with a dependency on SIC ~~for the distribution of cloud FoO during the different winter months~~in the monthly distribution. For MPC

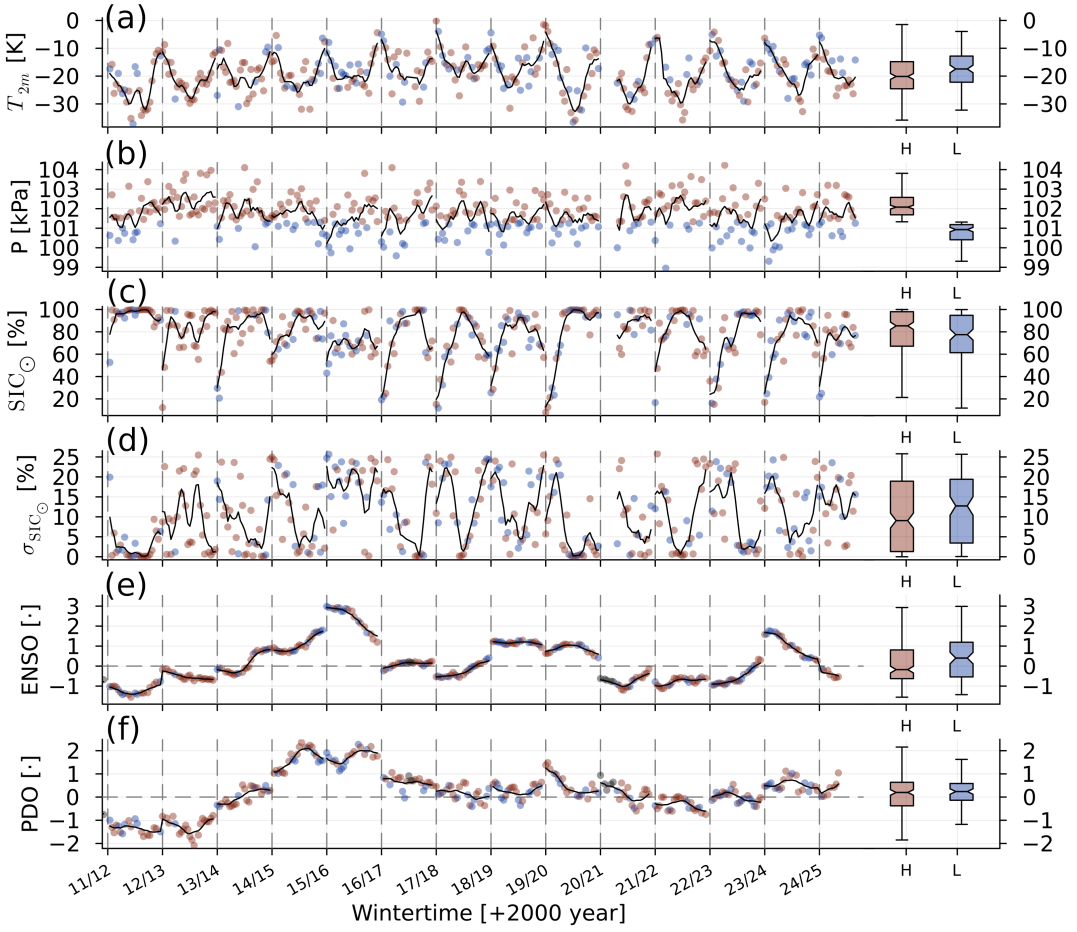


Figure 3. Wintertime climatology for the NSA site as time series from 2011 to 2024 for: (a) 2 m air temperature, (b) surface atmospheric pressure, (c) average $SIC_{\odot}$ within the whole 50 km semi-circle around NSA site, (d) standard deviation of $SIC_{\odot}$, (e) ENSO index, (f) PDO index. For visualization purposes the data is shown as weekly averages (circles), the solid black line is the weekly moving average. The vertical dashed lines indicate the jump from end of April to November, thus the apparent discontinuity at these lines is not physical. On the right of each panel the whole data distribution is shown as boxplot separated according to Eq. 2 for H- and L-pressure systems in light-red and light-blue, respectively.

(Fig. 4, right bars) the FoO ~~shows a reduction from start to end of winter from about~~ decreases from ~56% in November to ~~about~~ ~40% in April, with the largest contribution from SIC>95% ~~happening~~ occurring in January. ~~The total~~ Total cloud FoO (left bars) ~~were~~ is derived from all observations ~~of clouds~~ with CTH $\leq$ 3 km and either MWR-LWP > 0 $\mathrm{g\,m^{-2}}$ or IWP > 0 $\mathrm{g\,m^{-2}}$~~referring to cloud liquid and cloud ice detections. The~~ , indicating detection of liquid or ice clouds. MPC occurrence is ~~from where both the~~ defined by simultaneous detection of liquid and ice by both MWR and radar~~have detected liquid and ice simultaneously. The fact that for every month there are occurrences~~ . The persistent presence of SIC=0% ~~, indicates the~~

~~constant presence~~ in every month indicates the continuous occurrence of polynyas and leads during ~~wintertime~~ winter along the SIC semi-cone around the NSA site. It is important to note that the SIC ~~shown~~ values in Fig. 4 ~~is~~ represent the average within
330 ~~the semi-cone (~~a 50 km radius~~and ~~, 6° wide ~~)~~ semi-cone, with the azimuth ~~being determined by the WVT direction~~determined by direction of the maximum WVT.

The absolute values for total cloud and MPC are ~~in line with other studiessuch as Shupe et al. (2011) reporting~~ consistent with previous studies: Shupe et al. (2011) reported an annual total cloud FoO of ~~around~~ ~80% at NSA~~and Shupe et al. (2006) reporting~~ , and Shupe et al. (2006) reported a MPC FoO of ~~around~~ ~40% ~~at NSA~~ in fall.

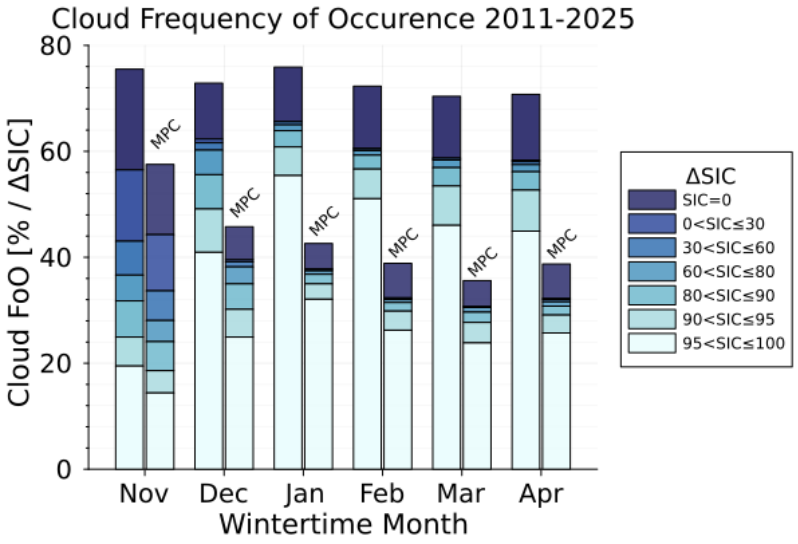


Figure 4. FoO for total (left bars) and mixed-phase clouds (right bars) per month for wintertime from 2011 to 2025. The FoO is based on cloud events in a month versus total days in a month.

335 To investigate the relationship ~~of sea ice with~~ between sea ice and cloud properties, the data ~~are sorted as a function of SIC with a bin width centred~~ were binned by SIC with bins centred at every 20^{th} percentile. ~~The MPC property is~~ MPC properties are represented by the median $\mu_{1/2}$ and its MAD σ_{mad} ~~of its distribution contained within a specific~~ within each SIC bin. ~~Note that for~~ For the following analysis~~the~~ , MPC detection were ~~constrained~~ restricted to cases with LWP and IWP above 5 $\mathrm{g\,m^{-2}}$ to reduce noise ~~due to the minimum detectable in the retrievals~~from minimum detectable retrieval uncertainties, similar as in
340 PSG23~~method~~.

Figure 5 presents the liquid water path (LWP), cloud droplet effective radius r_{eff}, ice water path (IWP), and ice particle effective radius r_{eff} as ~~a function of the~~ functions of upwind sea ice concentration along ~~the~~ $\pm 3°$ of the maximum $\nabla_z \mathtt{WVT}$ direction. Observations ~~from~~ under H-pressure systems are shown on the left ~~side~~ (Fig. 5 a,c,e,g), and L-pressure on the right ~~side~~ (Fig. 5 b,d,f,i). ~~The upwind coupled/decoupled~~ Coupled (blue-circles) and decoupled (orange triangles) cases are
345 indicated~~by blue-circles/orange-triangles, respectively. For clarity, circles and triangles belonging to~~ , with data points from the same SIC bin ~~are displaced~~ offset by -3% ~~.~~ for clarity.

To describe the data behaviour, the ~~empirical model's best fit is indicated by the~~ best fit empirical model is shown as solid coloured lines, with the 95% confidence interval (CI) ~~is marked as shadowed area around the solid lines along with the~~ shaded around them. The coefficient of determination r^2 and ~~goodness of fit~~ goodness-of-fit χ^2 are provided for coupled (blue) and decoupled (orange) cases, as defined in App. A, Eq. A3 and Eq. A2, respectively.

The results in Fig. 5 reveal ~~the tendency for~~ that several microphysical cloud properties ~~to~~ increase in magnitude as SIC decreases. ~~It has been found that the best empirical model representing the described behaviour~~ The best-fitting empirical model is given by Eq. 3~~with a maximum trending to~~ , which asymptotically approaches $\beta_1 + \beta_2$ ~~for~~ as SIC$\rightarrow$0%. This empirical model ~~has been chosen specifically to best fit the coupled cases, thuswhen the fit is not the best~~ was specifically optimized for coupled cases; thus, poor fits for decoupled cases ~~it is an indicator for the difference between coupled/decoupled cases~~highlight differences between coupling regimes. For decoupled cases, only few cloud properties ~~have a clear relation with SIC. For many variables no correlation was found~~show a clear relationship with SIC, and many variables exhibit no significant correlation.

$$\mathcal{F}_{var}(\mathrm{sic};\boldsymbol{\beta}) = \beta_1 + \beta_2 \exp\left(\mathrm{sic}^2\right) \tag{3}$$

where sic $\in \{0,\ldots,1\}$ is ~~the~~ normalized sea ice concentration, $\mathcal{F}_{var}$ is the observed cloud property ~~to be examined as a function of sic (for instance~~ (e.g. LWP, IWP, droplet r_{eff}, ice particle r_{eff})~~.~~ , and β_1, β_2 are ~~the empirical coefficients obtained from the best~~ empirically derived coefficients from non-linear curve ~~fit. In this study~~ fitting. Eq. 3 was ~~favoured over the power law function proposed as~~ preferred over the power-law form $\mathcal{F} = aSIC^b$ ~~by~~ (PSG23~~. The reasoning for that is that during MOSAiC wintertime the observed SIC were mostly~~) because the MOSAiC wintertime observations were predominantly above 90% ~~(with sparse cases of SICbetween 80% and 90%). Contrarily, the present study covers SIC observations ranging~~ SIC, whereas this study spans SIC observations from 0% to 100% ~~during the 14 years~~ over 14 years , providing a more complete picture ~~for the sensitivity~~ of cloud properties ~~to change as a function of~~ sensitive to SIC.

Specifically~~in~~ , Fig. 5 ~~,~~ panels (a) and (b) reveal a clear ~~relationship between LWP and~~ increase in LWP with decreasing SIC in coupled cases ~~: LWP~~ (blue circles)~~increases as sea ice coverage diminishes. Specifically, LWP increases steadily until it levels-off~~ , levelling off at a median ~~value~~ of $\sim$80 to 120 $\mathrm{g\,m^{-2}}$ for SIC$\lesssim$30%. ~~Moreover, when~~ When the observations are sorted according to ~~the presence of H- or L-pressure weather systems at NSA site, further differences are found. For instance, the data fits~~ weather system, the fit to Eq. 3 ~~better for the H-pressure~~ is better for H-pressure case s(r^2=0.80 and χ^2=0.1) ~~, than for the~~ than for L-pressure cases (r^2=0.80 but χ^2=0.34). ~~In addition, for~~ For L-pressure, LWP ~~data is more variable which results~~ exhibits higher variability, resulting in larger uncertainties ~~for the~~ in β_1 and β_2 ~~parameters~~ in Eq. 3 (~~i.e. wider shaded area around best fit line~~ wider shaded CI in Fig. 5 (b)), ~~especially~~ particularly due to outliers ~~that can be spotted at around~~ near 90-80% SIC. The ~~found behaviour of LWP for decoupled cases~~ decoupled LWP behaviour (orange triangles), ~~is in agreement with findings by Saavedra Garfias et al. (2023)confirming that LWP in decoupled scenarios does not follow any~~ align with Saavedra Garfias et al. (2023), confirming no significant relationship with SIC. This is supported by ~~largely~~ reduced r^2 of 0.51 ~~/~~(H-pressure) and 0.52 ~~for H-/L-pressurecases, respectively. Droplet effective radius r_{eff} (~~(L-pressure). Similarly, droplet effective radius (r_{eff}; Fig. 5 (c) and (d)) shows ~~similar behaviour as LWP, with the coupled droplet r_{eff} being strongly~~

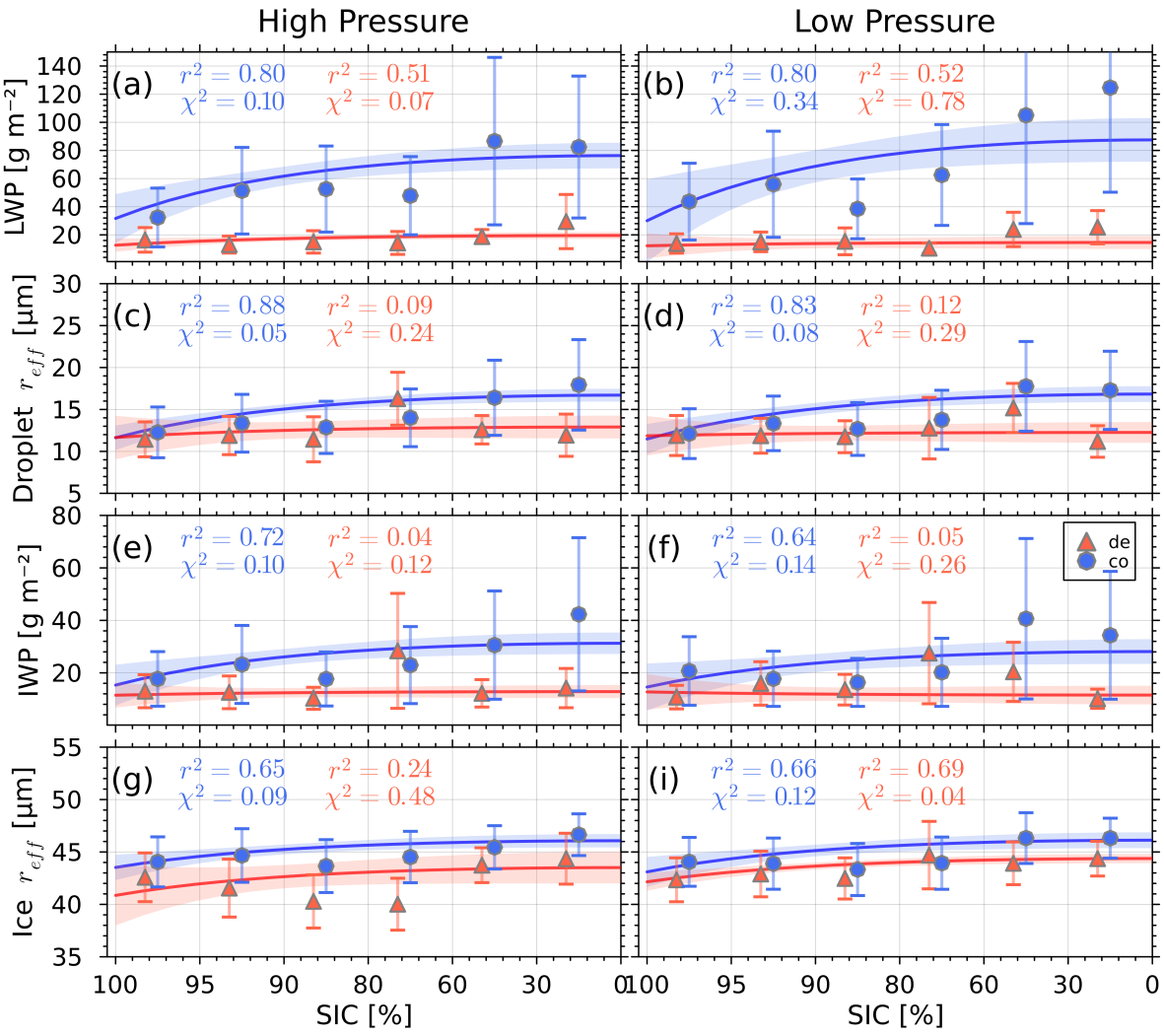


Figure 5. Cloud microphysical properties as a function of SIC (for SIC>5%) for coupled (blue circles) and decoupled (orange triangles) classes during the wintertime period from 2012 to 2024. H-/L-pressure systems are arranged on the left/right columns, respectively. Liquid water path (a, b); droplet effective radius (c,d); ice water path (e,f); ice effective radius (g,i). Symbols/bars represent the median/$\pm\sigma_{\text{mad}}$ for the distribution within SIC bins of every 20^{th} percentile. Lines indicate the best fit with 95% confidence interval (CI) shading around the solid lines. The r^2 and χ^2 are the best fit indicators for the model Eq. 3 for coupled/decoupled. Note that x-axis ticks and labels are not equidistant.

380 ~~negatively correlated with SIC . At the same time, droplet r_{eff} was not found to be correlated with SIC for decoupled MPC clouds~~a strong negative correlation with SIC in coupled cases, but no significant relationship in decoupled cases.

Regarding IWP ~~,~~ (Fig. 5 (e) and (f)~~contrast the MOSAiC findings that IWP does not exhibit any change in relation with different SIC values. Instead, at NSA site a high correlation between increasing IWP in decreasing SICsituations was found~~

for coupled cases with) no consistent change with SIC is observed in general. However, coupled cases show a strong positive correlation with decreasing SIC, particularly under H-pressure systems (r^2 as high as = 0.72for H-pressure cases. For decoupled cases however, IWP does not present any). Decoupled cases show no statistically significant difference as SIC changes . Within a changes with SIC. These findings are consistent with pan-Arctic perspective and from satellite observations Cesana et al. (2024) found out that for winter time the cloud cover classified as ice increases as SIC decreases (negative correlation), and cloud cover classified as satellite observations by Cesana et al. (2024), who reported a negative correlation between SIC and ice cloud cover, and mixed-phase are even strongly negative correlation with SIC, which is in agreement with our results, albeit the temporal and spacial scales of both studies are differentcloud cover, though differences in spatial and temporal scales exist.

In coupled scenarios, the For ice effective radius (Ice r_{eff}, Fig. 5 (g) and (i))shows , a significant relationship with SIC when fitted to Eq.3 as it is indicated by their is observed in coupled cases (r^2=0.65/0.66 and χ^2=0.09/0.12 (Fig. 5 (g) and (h) for H-pressure for H- and L-pressure cases), respectively. However, the change in magnitude of ice particle r_{eff} for changing SIC is less pronounced compared to cloud though the magnitude of change is smaller than for droplet r_{eff}. Interestingly, for ice r_{eff} in decoupled situationsIn decoupled cases, a similar relationship is observed albeit with more widely scattered data that reduces the trend is observed but with greater scatter, reducing r^2 to 0.24 for H-pressure cases. Moreover, decoupled LWP, IWP, droplet r_{eff}, and ice r_{eff} have systematically lower values as their counterparts in coupled situations. systems. Notably, all MPC macro- and micro-physical properties are systematically lower in decoupled cases compares to their coupled counterparts.

A set of Key MPC macrophysical properties are displayed in Fig. 6: Cloud geometrical depth (δ_h: cloud top minus cloud base heights) in δ_h =CTH - CBH; Fig. 6 (a) and (b)), liquid layer cloud base height (CBH) in ; Fig. 6 (c) and (d)), cloud top temperature (CTT) in ; Fig. 6 (e) and (f), and cloud layer), and cloud-layer temperature lapse-rate (Γ_{cloud}) in ; Fig. 6 (g) and (i)).

Fig. 6 reveals that mostly decoupled MPCmacrophysical properties and SIC have For decoupled MPC, no clear correlation with SIC is evident. This is e.g. evident from the coefficient of determination reflected in low r^2 of values (0.38 for δ_h and of , 0.15 for CBHespecially for MPC observed in H-pressure system situations, respectively. For coupled MPC cases a clear relationship of) under H-pressure systems. In contrast, coupled cases show a clear decrease in δ_h and SIC is found, with cloud depth tending to decrease as SIC decreases with decreasing SIC (r^2=0.63). With reference to the results , indicating shallower clouds. These results confirm findings from the MOSAiC expedition, the findings that can be confirmed are: for coupled : coupled MPC are generally thicker and have lower CBH than decoupled casesδ_h/CBH are thicker/lower than their decoupled counterparts, independent of SIC with the exception of except for higher liquid CBH in coupled cases when H-pressure are present. under H-pressure systems.

The results for CTT (Fig. 6 (e) and (f)) show some statistically significant difference between coupled /decoupled cases. Nonetheless, shows significant differences between coupled and decoupled cases, with a noticeable dependency to SICcan be identified, with on SIC: colder CTT for sea ice covered ice-covered ocean and warmer CTT for large areas of open water(see Fig. 6 (e, f)). The model over regions with open water. The model (Eq.3fits better in decoupled cases) fits decoupled cases

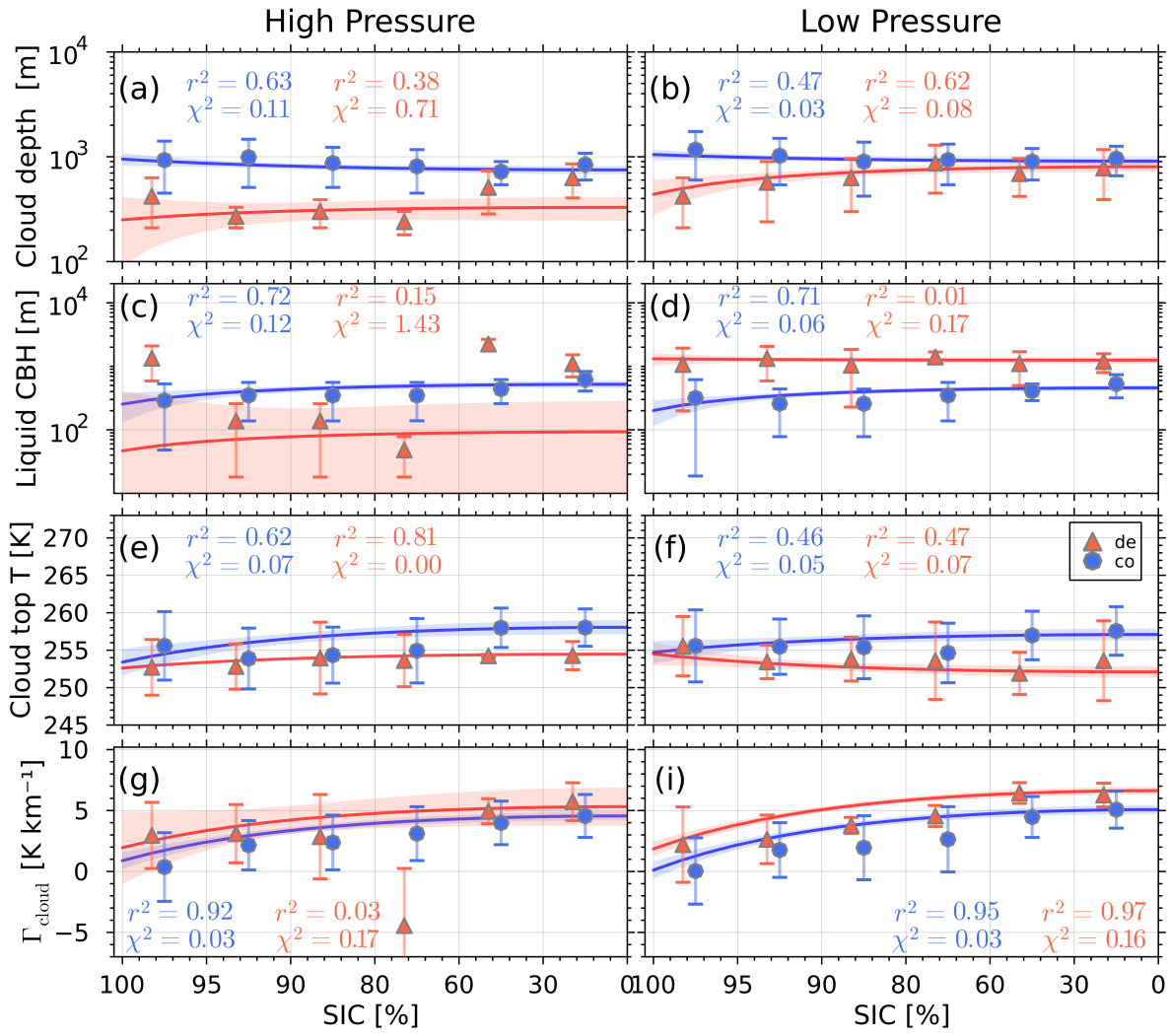


Figure 6. Same as Figure 5 but for cloud depth (a, b); liquid layer cloud base height (c,d); cloud top temperature (e,f); cloud layer temperature lapse-rate (g,i). Symbols (bars) represent the distribution's median (±MAD) for SIC bin widths at every 20^{th} percentile.

better (r^2=0.81 and H-pressure) ~~as compared to~~ than coupled cases (r^2=0.62). ~~For coupled cases , CTT is generally slightly higher than for~~ Coupled cases generally exhibit slightly higher CTT than decoupled cases.

The cloud-layer temperature lapse-rate ~~within a cloud layer is defined as~~ ($\Gamma_{\text{cloud}} = -\sum_{z=CBH}^{CTH} \left(\frac{T_{z+1} - T_z}{H_{z+1} - H_z}\right)$ ~~, is the single~~) is the only macrophysical property that ~~poses a pronounced modulation of its magnitude as a function of~~ showed pronounced modulation by SIC (Fig. 6 (g) and (i)). ~~The Γ_{cloud} under H- and L-pressure systems depicts a systematic bias with Γ_{cloud} for decoupled cases having larger values than the~~ Decoupled cases show systematically larger Γ_{cloud} values than coupled cases. ~~Moreover, Γ_{cloud} observations are well represented by the empirical model~~ The empirical model (Eq. 3) fits the data with

a robust coefficient of determination of r^2=0.95 and χ^2=0.03 for the L-pressure and coupled cases. ~~The dynamic of Γ_{cloud} ascribed by SIC suggests that for conditions with dominant sea ice coverage (~~For H-pressure and L-pressure systems with SIC$\gtrsim$95%~~for H-pressure and L-pressure systems) the coupled lapse-rate median~~ , the median Γ_{cloud} (blue dots in Fig. 6 (g) and (i) SIC>95%) shows that ~~about the~~ approximately half of the ~~Γ_{cloud} distribution is found to be negative . This implies~~ distribution is negative –indicating a temperature inversion within the cloud layer ($T_{top} > T_{base}$). ~~When SIC decreases~~ As SIC decreases (e.g. SIC<95%), Γ_{cloud} becomes clearly positive (i.e. $T_{top} < T_{base}$)~~meaning the cloud temperature cools with height , resembling~~ , indicating cooling with height and a tendency towards a moist adiabatic ~~process~~lapse-rate.

The ~~behaviour of micro- and macro-physical properties as a function of SIC suggest that as SIC decreases shallower clouds are observed (Fig. 6 (a,b)), at the same time higher~~ results suggesting an apparent contradiction that shallower clouds with increasing LWP and IWP ~~are found~~ as SIC decreases~~(Fig. 5 (a,b,e, f)). That apparent contradiction is realized by the increase of~~ , is resolved by the concurrent increase in liquid- and ice r_{eff} ~~with the decrease of SIC~~ (Fig. 5 (c,d,g,i)). Furthermore, ~~it was found that the lower atmosphere~~ surface air temperature (T2m) ~~positively correlates some of the MPC's~~ shows a positive correlation with several micro- and ~~macro-properties, mainly for~~ micro-physical properties, particularly in coupled cases. The physical explanation for the observed increase in LWP and IWP with the decrease of SIC (i.e. warmer surface) ~~is given by the fact that SIC decrease (T2m increase) indicates that more~~ lies in enhanced latent and sensible heat fluxes ~~are released by opening in the seaice to the lower atmosphere, favorable for~~ from sea ice openings, which promote convection and sea salt ~~release, and when that is coupled to the cloudsit drives the increase of the MPC parameters. These findinds are aligned~~ aerosol release. When coupled to clouds, this drives increased cloud water content. These findings align with in-situ measurements in Svalbard, which suggesting that a warming Arctic ~~favours the increase of highly active~~ enhances ice nucleating particles, ~~thus allowing the~~ enabling formation of ice-containing clouds at warmer ~~temperature~~ temperatures (Tobo et al., 2024). Similarly, Schäfer et al. (2025) ~~using~~ found in Arctic MPC simulations ~~found an increase in~~ that a warming climate increases cloud ice water content ~~with a warming climate due to the increase of~~ via enhanced ice-nucleating particles and ~~the rime splintering process and~~ secondary ice production (e.g. rime splintering).

3.2 Year-to-year variability and trends

~~In this section,~~ MPC properties are ~~clustered for each considered winter and then analysed as time series to study year-to-year variability and/or trends. No separation for SIC variation has been made here. Each data point in the time series is comprised of descriptive statistics from the distribution of observations from a given wintertime referred to using the nomenclature~~ analysed as a time series across 14 years wintertime (WT) seasons $WT = \{2011/12, 2012/13, \ldots, 2024/25\}$, with each data point representing descriptive statistics (median, MAD) from observations within a given WT (e.g. "2012/13" ~~to represent, for example, wintertime (WT) from~~ = 1st November, 2012 to 30 April, ~~2013. The time series is composed of 14 years denoted as $WT = \{2011/12, 2012/13, \ldots, 2024/25\}$, and the MPC micro- and macro-physical properties are studied as a function of WT~~2013). No SIC-based separation is applied here.

A first attempt to analyse MPC time series observations at NSA site has been reported by Saavedra Garfias and Kalesse-Los (2024)~~for only~~ . They previously analysed a 10 year subset of coupled/decoupled ~~classes for a shorter period of 10 years.~~

Firstly, these preliminary findings stressed MPC at NSA site, reporting the oscillatory nature of the magnitude of some MPC properties with time . Secondly, a lack of but no statistically significant trends which were estimated directly using Ordinary Linear Regression (OLR)from the wintertime average was reported. That trend estimation approach, however, suffers of . However, OLR is limited by two major shortcomings: i.e. heteroskedasticity (increased variance with higher median values) and residuals' bias with skewed distributions . Both make the applicability of OLR questionable. Heteroskedasticity happens due to a distribution's variability being higher when the median values are larger; i.e. the larger the median LWP the wider its variance in a given wintertime. The second shortcoming occurs due to the oscillatory time series, edue to oscillatory signals –e.g. , a local maximum LWP was found at 2016/17 between two local minima in 2013/2014 and 2018/2019 respectively. This results in the regression residuals to be biased with skewed distributions towards large LWP values, i.e. residuals do not adhere to a normal distribution with population mean of zero. 2019– violating OLR's assumption of normally distributed residuals.

To overcome these shortcomingsthe oscillatory nature of the signal needs to be considered. This is achieved by exploring two commonly used methods in time series analysis (Chang et al., 2021): address these shortcomings, two robust methods are applied, both using weighted linear regression (WLR) with weights inversely proportional to the variance (Eq. A1) within wintertime (Chang et al., 2021):

i. the oscillatory magnitude is eliminated by using a moving window average over all time series data points with an running window of : A 10 years. For example, the data point for year running window smooths the time series (e.g. 2016/17 is averaged over ± 5 winter seasons. Then winters), then a weighted linear regression (WLR) is applied. The WLR is an efficient way for fixing heteroskedasticityin linear regressionThis reduces noise and mitigates heteroskedasticity.

ii. the signal is considered to follow : The signal is modelled as following a natural cycle with a frequency occurring within the 14 years period. For example, oscillations alike any Arctic intradecadal climate variability that has the potential to modulate the sea ice or cloud properties. In this case a A fixed frequency ν_k [yr^{-1}] is applied to fit the data via non-linear regression with cyclical terms (Harmonic functions) needs to be appliedfollowing Eq. 4.

In both methods the distribution variance of Both methods use weighted regression to account for varying cloud properties within a wintertime period is taken into account by applying a weighted regression, with the weights being proportional to the inverse of the variance as given by Eq. A1 where $\sigma \equiv \sigma_{\mathrm{mad}}$ when the fitting is performed over the median $\mu_{1/2}$ or the standard deviation when the mean is used. variability. The time series WLR fitting model to be applied for the methods ***i*** and ***ii*** are given by:

$$\mathcal{Y}(t;\boldsymbol{\beta}) = \begin{cases} \beta_1 + \beta_2 t + \varepsilon & \text{method } \boldsymbol{i}. \quad (4a) \\ \beta_1 + \beta_2 t + \beta_3 \cos(2\pi\nu_k t - \beta_4) + \varepsilon & \text{method } \boldsymbol{ii}. \quad (4b) \end{cases}$$

where $\mathcal{Y}(t;\boldsymbol{\beta})$ is the time dependent cloud parameter to be fitted (e.g. LWP, IWP, cloud droplet/ice particle r_{eff}, etc.)in accordance with method ***i*** or ***ii***.In Eq. 4, t runs over the sequence of wintertime WT and the coefficient to fit is denoted by the vector $\boldsymbol{\beta} = [\beta_1, \beta_2, \ldots]$, and ε represents the model residuals. In both Eq. 4a and 4b the time series trend is determined from $\frac{\Delta \mathcal{Y}}{\Delta t} \equiv \beta_2$. For Eq. 4b, ν_k is an extra parameter, with units of yr^{-1}, that represents the represents the dominant frequency of the

oscillating signal with phase shift β_4. Note that in Eq. 4b, ν_k is not ~~an element of the fitting coefficients vector β~~ determined by the regression but rather a so-called "free parameter"~~, i.e. its value is not determined by the regression's best fit from the time series data. Instead it~~ . ν_k is obtained from an external source; the selection of this free parameter is presented in detail later in Sec. 3.2.2.

~~In the following, the results from time series analysis is presented according to methods *i* (~~The results are presented in Sec. 3.2.1 ~~) and *ii* (~~(method *i*) and Sec. 3.2.2 (method *ii*), followed by a ~~comparison of the results by both methods~~comparative analysis.

3.2.1 Method *i*: Trend estimation using moving-average time series

~~Using the time series of MPC properties after smoothing the data by the moving average~~method, the data is After smoothing the MPC time series with 10 year moving average, data are fitted to Eq. 4a ~~by applying~~ using WLR. The trend is ~~then assumed to be the fitted parameter~~ derived from the fitted coefficient β_2, and the results are ~~assorted~~ sorted by the cloud coupling class and pressure system at NSA site.

Figure 7 depicts the time series of selected MPC properties that exhibit the largest variability along the years~~, namely~~ : LWP, liquid CBH and CTT. ~~As in previous figures the MPC properties are separated by coupled~~ Coupled (blue circles), and decoupled (orange triangles) ~~status and~~ case are separated by pressure system. ~~A distinctive variabilityof LWP per wintertime is evident, which is reflected by the magnitude of the trendsfor coupled LWP of~~ LWP exhibits strong inter-annual variability. Coupled LWP shows significant positive trends: +4.4±0.7 g m^{-2} dec^{-1} ~~for~~ under H-pressure and +24.3±0.7 g m^{-2} dec^{-1} ~~for L-pressure in~~ under L-pressure (Fig. 7 (a) and (b)~~, respectively. The decoupled LWP confirm the systematically lower values compared to the coupled counterparts (as in Sec. 3.1)in this time series perspective~~). Decoupled LWP ~~also show more stochastic variability~~remains lower overall and displays higher stochastic variability, resulting in a less pronounced and negative trend ~~for L-pressure system~~ of -5.3±0.7 g m^{-2} dec^{-1} under L-pressure.

~~The liquid layer CBH time series is shown in~~ Liquid layer CBH also shows clear trends (Fig. 7 (c) and (d)~~. This property also has a noticeable evolution along the years for H- and L-pressure systems, with the first having similar positive trends~~). Under H-pressure, both coupled and decoupled CBH increase at similar rates (+54.3±0.7 m dec^{-1} ~~) and (~~and +54.9±1.0 m dec^{-1}~~)~~ ~~for coupled and decoupled CBH, respectively; whereas CBH for L-pressure~~depicts the opposite trends (coupled: ~~almost no trend with~~ , respectively). Under L-pressure, trends reverse: coupled CBH shows small change (+7.5±0.7 m dec^{-1}~~, decoupled:~~), while decoupled CBH decrease sharply (-134.5±0.8 m dec^{-1}).

~~Similar as in Sec. 3.1, Fig. 5 for variable SIC regimes, CTT does not show a distinct magnitude difference for coupled and decoupled cases, the same is found in time series basis~~ CTT (Fig. 7 (e) and (f)) shows no significant difference between coupled and decoupled cases, consistent with Sec. 3.1. In general, ~~the wintertime CTT median has the tendency to~~ CTT median values slightly decrease over time, ~~albeit the strength of that reduction depends on the coupled status and pressure system. The largest reduction happens for~~ with the strongest reduction under H-pressure and coupled cases (trend: -1.6±0.6 K dec^{-1})~~and the lowest for L-pressure decoupled cases with a~~ , and the weakest (non-significant~~trend of~~) trend under L-pressure and decoupled cases (-0.9±0.8 K dec^{-1}).

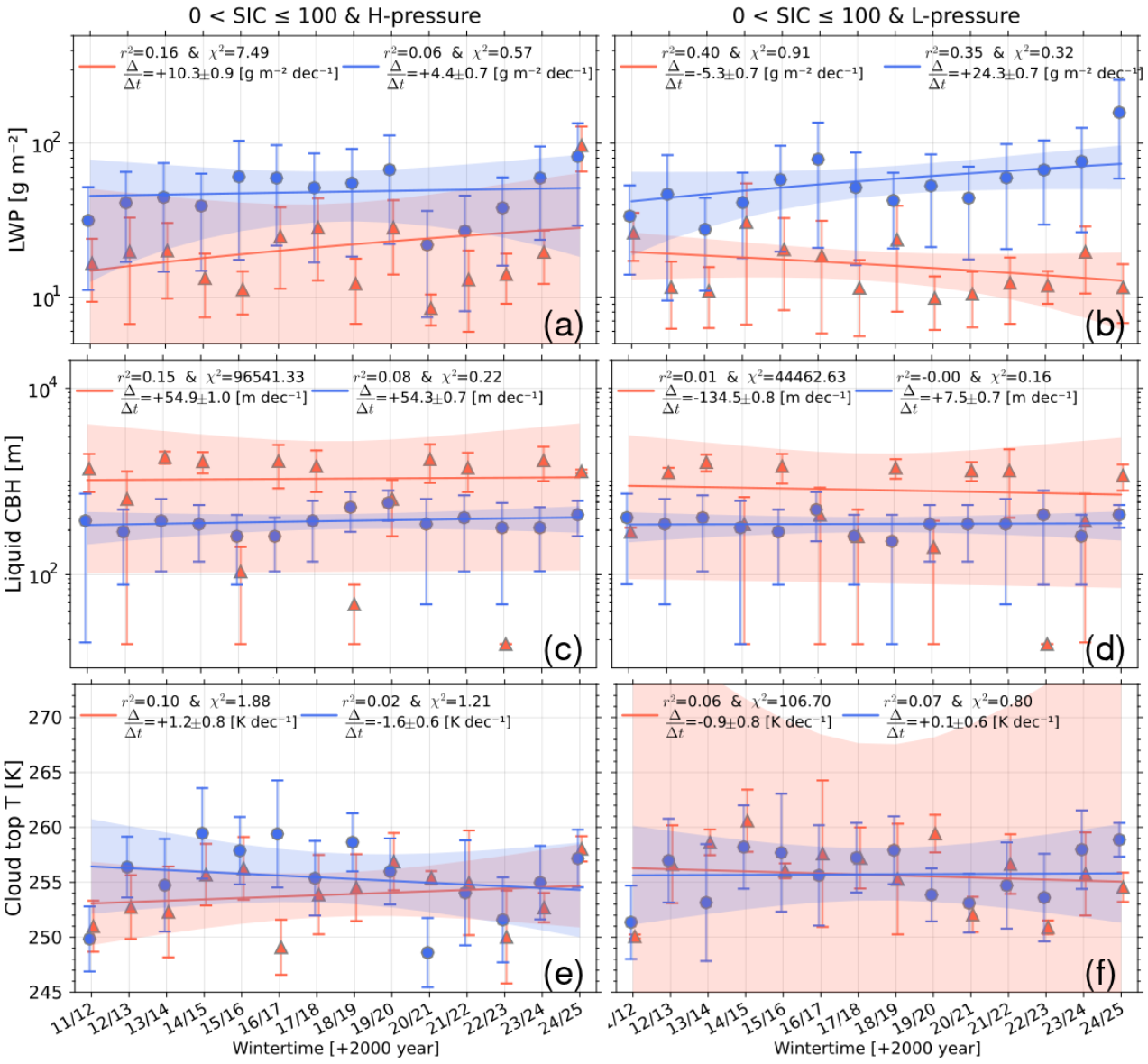


Figure 7. MPC time series for coupled (blue circles) and decoupled (orange triangles) represented by the median ($\mu_{1/2}$) and σ_{mad} (bars) of wintertime distributions. H-pressure (left column) and L-pressure (right column) for LWP (a, b), liquid layer CBH (c, d), and cloud top temperature (e, f). The linear trends (± uncertainty) are indicated with the solid lines (shared area is 95% confidence interval) and trend values in units per decade, the coefficient of determination r^2, and χ^2 are presented in legend.

3.2.2 Method *ii*: Trends estimation considering cyclical time series

Given the oscillatory nature of ~~observed time series of MPC properties, first~~ MPC time series ~~–~~first reported by Saavedra Garfias and Kalesse-Los (2024)~~, in the present study we propose the hypothesis that those oscillations might be induced by the climate variabilityat intra-decadal time scales. Generally speaking, climate~~ –, we hypothesize that these oscillations are driven by intra-decadal climate variability. Climate teleconnections can influence ~~the formation or melting of sea ice in the Arctic, as a result of which MPC propertiesare changed according to the findings from previous~~ Arctic sea ice formation/melting, thereby modulating MPC properties, as shown in Sec. 3.1. ~~That might imply the observed MPC time series fluctuations can be explained by the modulation of relevant climate modesin the Arctic. The motivation to postulate this hypothesis is twofold~~This suggest that observed MPC fluctuations may be linked to large-scale climate modes. The hypothesis is supported by two lines of evidence: Firsty, ~~there are numerous studies supporting~~ extensive literature confirms climate teleconnections between ~~the~~ Tropical Pacific, sub-tropical regions and the Arctic (Timmermann et al., 2018; Kodaira et al., 2020; Zhang et al., 2023; Deng and Dai, 2024; Zhong et al., 2024)~~. Secondly, a noticeable pattern of~~ ; and secondly, MPC time series ~~that resembles the~~ (e.g. LWP, CTT, δ_h, and CBH) exhibit patterns resembling ENSO or PDO ~~evolution along the study period; for instance, Fig. 7 (a) and (b) where LWP time series present a crest closely aligned~~ cycles –e.g., LWP peaks align with strong El Niño events (positive ENSO in 2016 and 2023~~in Fig. 3). Conversely LWP time series' minima show parallels to~~), and minima with La Niña events (negative ENSO in 2020 to 2022)~~. Similar patterns can be observed for CTT, δ_h, etc., or even with a certain difference in phase (e.g. CBH) and varying intensity of the oscillation.~~ , with phase shift and amplitude differences across MPC variables.

~~Since no absolute certainty can be obtained about which single or combination of climate modes are modulating the MPC observations, three common indicesare considered, namely~~To test this, we consider three major climate indices: Arctic Oscillation (AO), PDO, and ENSO. ~~In Eq. 4b the~~ The free parameter ν_k (frequency of signal ~~) was selected among a set of frequencies in Eq. 4b) is selected~~ from relevant harmonics of these ~~three climate indices. The set of values for ν_k was obtained after a~~ indices, identified via discrete Fourier analysis performed over the ENSO, PDO and AO signals (details in App. D). Only frequencies ~~associated with strong Fourier components (~~with Fourier amplitudes larger than 100 ~~) were considered to be relevant~~ were considered (red triangles over the x-axis of Fig. D1 (c) in App. D): ν_k={0.093, 0.155, 0.186, 0.217, 0.248, 0.279, 0.341, 0.434} yr^{-1}~~which corresponds~~ , corresponding to periods of {10.8, 6.5, 5.4, 4.6, 4.0, 3.6, 2.9, 2.3} yr ~~, values in agreement with other more extensive analysis i.e.~~ consistent with know climate modes e.g., 2.8, 4.3, and 5.7 yr ~~period for AO, plus~~ for AO; 12 yr for ENSO; (Zhang and Moore, 2011). All ν_k values are common harmonics for ENSO, PDO and AO, ~~albeit with various levels of contribution to the climate indices. The~~ though with varying levels of contributions. For each ν_k, the time series are fitted to Eq.4b~~using all values of ν_k (e.g. six fitted curves), and the~~ , and three goodness of fit ~~parameters are calculated, namely~~ metrics are calculated: χ^2, coefficient of determination r^2, and the normalized root mean square error nRMSE. ~~Then the best~~ The optimal ν_k is ~~determined by minimizing~~ selected via a cost function (Eq. A5) ~~dependent of~~ minimizing χ^2 ~~,~~ and nRMSE while maximizing r^2 ~~, and nRMSE . The corresponding parameter definitions and description of the procedure can be found in~~ (see Appendix A1 and Fig. A1 for ~~LWP and CTT as examples~~example).

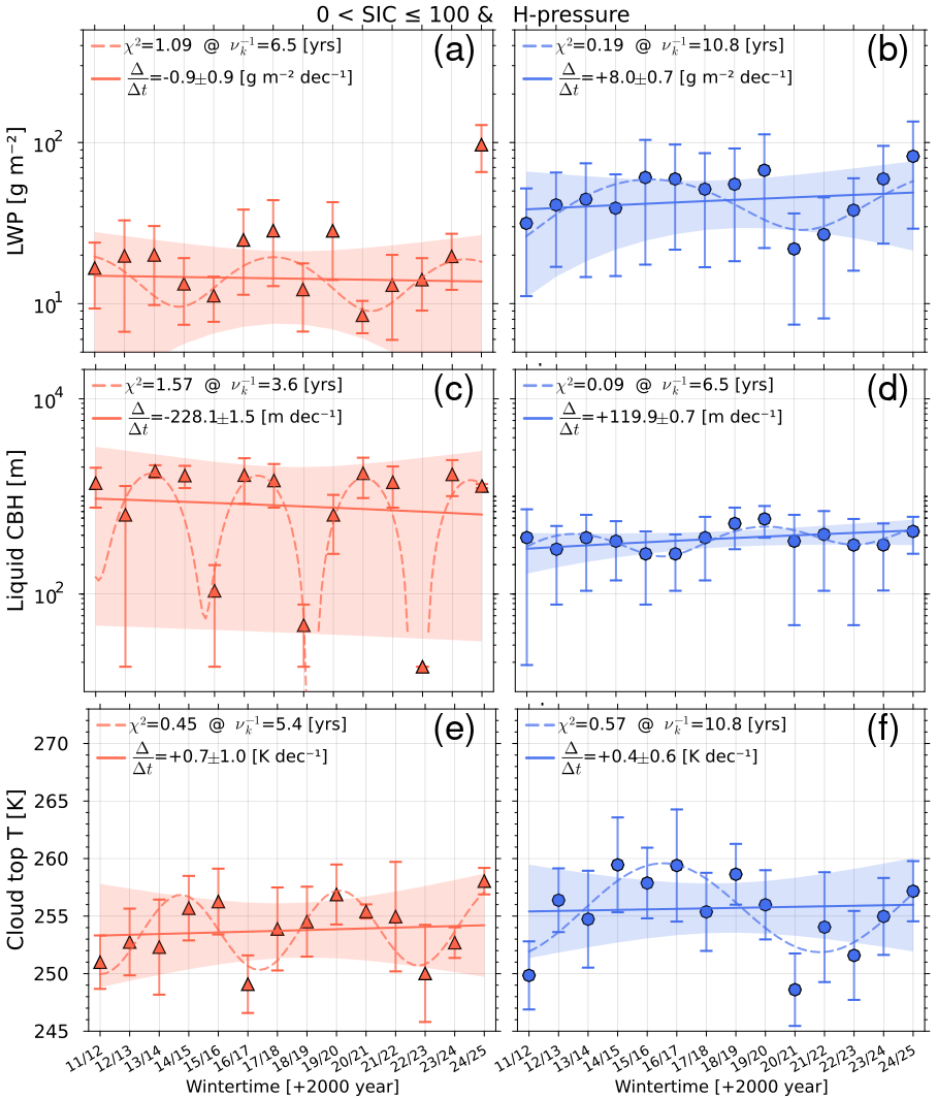


Figure 8. Same as in Fig. 7 but applying method *ii* for H-pressure systems. With LWP (a) and (b), liquid layer CBH (c, d), and CTT (e, f). Left column panels (a,c,e) show decoupled MPC (orange triangles) cases and right column (b,d,f) coupled MPC cases (blue circles). The best fit curves are dashed-lines and linear trends are the solid lines (shared area is 95% CI). The goodness of fit coefficient χ^2, the period of the cyclical curve ν_k^{-1}, and trend values, in units per decade, are indicated in legend.

560 The time series of MPC properties fitted to Eq. 4b to obtain the coefficients β are shown in ~~Fig.~~ Figure 8 for H-pressure systems~~, while the cases for L-pressure systems are presented~~ ; L-pressure results are in Appendix Fig. B1. The ~~fitting to Eq. 4b is performed for all values of ν_k, then a single frequency ν_k is selected based on the goodness of fit test (shown as legend in Fig. 8) which, along with the set of~~ best-fit frequency (ν_k in legend) and corresponding β ~~parameters, represents the best fit for the data (dashed-lines~~ coefficients (dashed lines in Fig. 8) represent the optimal model.

From Fig. 8 (a) and (b) it can be seen that under H-pressure systems, decoupled LWP is better represented by a cyclical signal with a period of Under H-pressure systems:

- Decoupled LWP best fit by a 6.5 years, while coupled LWP by 10.8 years. That difference in periods together with the amplitude coefficients β, fitted to Eq. 4b in each case, yield to dissimilar trends ($\frac{\Delta}{\Delta t} = \beta_2$ in Eq. 4b)for decoupled year cycle (linked to AO/DPO), yielding a weak negative trend (-0.9±0.9 $\mathrm{g\,m^{-2}\,dec^{-1}}$)and coupled .
- Coupled LWP follows a 10.8 year cycle (strongly tided to ENSO/PDO), with a significant positive trend (+8.0±0.7 $\mathrm{g\,m^{-2}\,dec^{-1}}$)cases Moreover, based on the Fourier transform analysis of the climate indicators, the period of 6.5 year suggest that decoupled LWP is likely linked to AO and PDO while the coupled LWP has a stronger modulation by harmonics of ENSO and PDO. .

The liquid layer For liquid cloud base height CBH for wintertime MPC ((CBH; Fig. 8 c and d)shows a best fit for periodic signal with periods of :

- Decoupled CBH fits a 3.6 /6.5 years for decoupled/coupled, respectively. For decoupled cases, a negative CBH trend was found: year cycle, with a trend of -228.1±1.5 $\mathrm{m\,dec^{-1}}$. Contrarily, for coupled cases a positive liquid CBH
- Coupled CBH fits a 6.5 year cycle, with a trend of +119.9±0.7 $\mathrm{m\,dec^{-1}}$was found. Concerning cloud .

Cloud top temperature CTT (Fig. 8 e and f) a shows slightly positive, albeit not statistically significant trend is found for both non-significant trends (decoupled: +0.7±1.0 $\mathrm{K\,dec^{-1}}$, and coupled: +0.4±0.6 $\mathrm{K\,dec^{-1}}$)cases, with good fit to periods of 5.4 and 10.8 years respectively. From the three climate indices analysed in Appendix D, the period of), best fit by 10.8 years is intelligibly present in the PDOand ENSO power spectra, with the strongest component belonging to PDO. A period of year (ENSO/PDO) and 5.4 years is the strongest signal for the year (ENSO) cycles, respectively. The 5.4 year cycle is the predominant intra-decadal ENSO variability, and the signal and second strongest for PDO, while non-present for AO but absent in AO (Appendix D).

3.2.3 Comparison of trends obtained by the two methods

The results for trends presented in Sec. 3.2.1 and Sec. 3.2.2 have been estimated considering data Trends were estimated for all SICconditions above zero. Additionally, the same procedure was performed considering subsets of SIC comprised by >0%, and separately for the lower and upper 50th percentiles of the total distribution of SIC. Those quantiles translate to two bins of SIC, i.e. the set of SIC = SIC: SIC ∈ { (0, 95], (95, 100] }%, for which their corresponding trends were estimated. Here the notation of, for example . The notation (0, 95], indicates that only data with 0%<SIC≤95%was used to perform the procedures shown in previous sections.

LWP trends for SIC subsets as indicated in the abscissae. The hollow symbols indicate the trend using method *i* (Eq. 4a), coloured symbols show results using method *ii* (Eq. 4b), grey shadows behind symbols indicate the trend is statistically significant (p<0.05), and the number next to the coloured symbols are the period in years for the best fit Eq. 4b. The colour bar

represents the goodness of fit χ^2 value. MPC observed in the presence of H-pressure systems in panel (a) and (c) for coupled and decoupled cases, respectively. MPC in the presence of L-pressure systems in panels (b) and (d) for coupled (upper row) and decoupled (lower row) cases, respectively. In . Results are summarized in Fig. 9the set of LWP trends as a function of SIC subset is summarized. The SIC on the-axis indicated as , where "All" corresponds to the results shown in refers to the full SIC range (Fig. 7 and Fig. 8. The coupled cases are presented on).

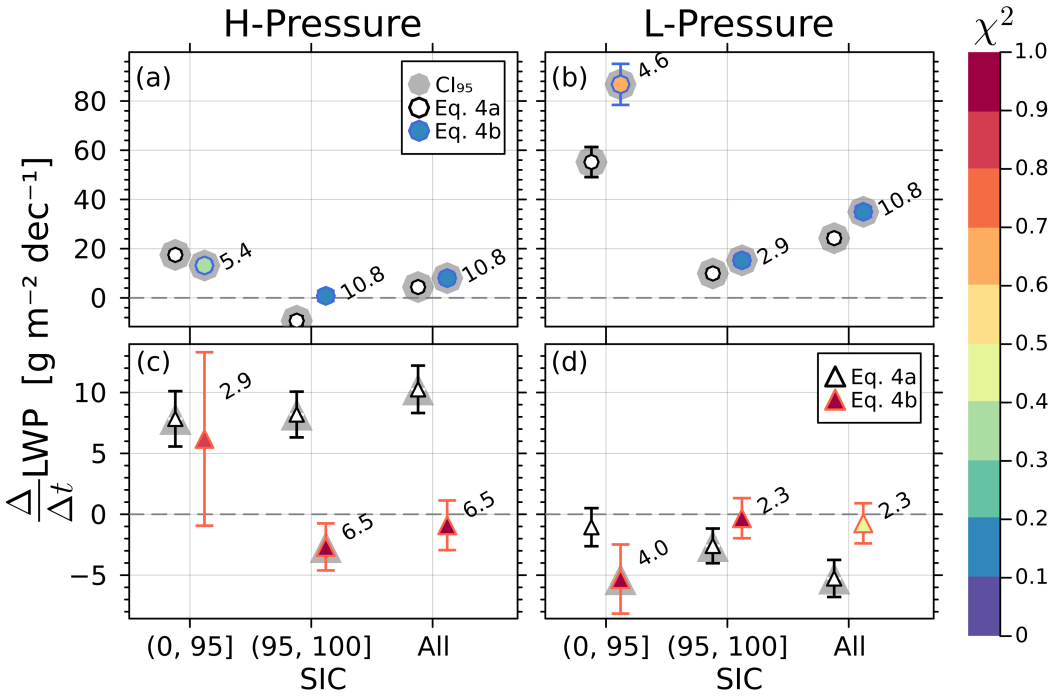


Figure 9. LWP trends for SIC subsets as indicated in the abscissae. The hollow symbols indicate the trend using method *i* (Eq. 4a), coloured symbols show results using method *ii* (Eq. 4b), grey shadows behind symbols indicate the trend is statistically significant (p<0.05), and the number next to the coloured symbols are the period in years for the best fit Eq. 4b. The colour bar represents the goodness of fit χ^2 value. MPC observed in the presence of H-pressure systems in panel (a) and (c) for coupled and decoupled cases, respectively. MPC in the presence of L-pressure systems in panels (b) and (d) for coupled (upper row) and decoupled (lower row) cases, respectively.

Coupled cases are shown in the top row of panels in Fig. 9 (a and b), while the decoupled cases on decoupled in the bottom row (c and d). The trends estimated using Eq. 4a (Hollow symbols represent method *i*) are hollow symbols , whereas the trends estimated fitting Eq. 4b ((moving average WLR); coloured symbols denote method *ii*) are the coloured symbols (harmonic fit), where the colour indicates the goodness of fit parameter χ^2 (the lower the value the better the ≡ better fit). Next to every coloured symbol the period related to the The period of best fit ν_k^{-1} in Eq. 4b is indicatedlabeled next to each coloured symbol.

It is noticeable from panel a and b in Fig. 9, that with respect to For coupled MPC-LWPthe coupled clouds' trends agree between the two methods , especially for , both methods agree well, especially under SIC>95%(50th percentile), while for ,

For SIC<95%~~the two methods start showing differences with an extreme value of~~ , discrepancies emerge: trends reach ≈ +55 (method *i*) and ≈ +86 $\mathrm{g\,m^{-2}\,dec^{-1}}$ ~~for SIC within~~ (method *ii*) under L-pressure in the lower 50th percentile ~~under L-pressure for methods *i* and *ii*, respectively. Most of the LWP trends in the coupled cases follow time series oscillation with periods of SIC. Most coupled LWP trends align with PDO/ENSO periods~~ (4.6, 5.4, and 10.8 years~~, characteristics for PDO and ENSO oscillations.~~).

~~On the contrary, for the decoupled clouds (panels c and d in Fig. 9)) a large variabilityof the trend values was found. Specifically for~~ In contrast, decoupled MPC-LWP shows high variability. Under H-pressure, method *ii* ~~, trends were found to reverse sign from positive to negative as the SICincreases when H-pressure systems are present over NSA site. LWP-trends for MPC in decoupled situations and under L-pressure system were slightly negative for both methods and low and high SIC~~ reveals a reversal in trend sign with increasing SIC –positive at low SIC, negative at high SIC. Under L-pressure, both methods yield slightly negative trends (Fig. 9 d). ~~The oscillation periods for decoupled cases are dominated mainly~~ Oscillations are dominated by AO and ENSO ~~signals~~ (i.e. 2.3, 2.9, 4.0, 6.5 years)~~and thus somewhat shorter~~ , with shorter periods than for coupled cases.

~~Regarding ice cloud~~ For ice properties, IWP ~~of coupled clouds does not have a statistically significant trend at L-pressure conditions, similarly Ice r_{eff} does not show any significant trend~~ (in coupled clouds shows no significant trend under L-pressure (method *i*), nor does ice effective radius (r_{eff}; Fig. S2 (b, c, d))~~when the moving average method is used. IWP only has a significant trend when the~~ . However, method *ii* ~~is used for trend determination. In that case IWP exhibits a positive trend at L-pressure affected by a~~ reveals a significant positive IWP trend under L-pressure (2.9 years ~~oscillation e.g. ENSO (~~ENSO cycle, Fig. S5 (b)) ~~, and at H-pressure a~~ and H-pressure (10.8 years ~~oscillation e.g.~~ ENSO/PDO cycle, (Fig. S4 (b)). This ~~suggest effects on cloud properties are likely due to~~ suggests that cloud responses are driven by weather patterns and ~~intrusions of warm air from low latitudes , a similar conclusion was found by Cesana et al. (2024) for~~ warm-air intrusions from lower latitudes –consistent with finding by Cesana et al. (2024) in the Bearing Sea using satellite observations.

3.3 ~~Discussion~~

4 Discussion and Summary

The findings presented in this study are the result of two approaches: first, an extension of the PSG23 method from one winter of observations during the MOSAiC expedition in the Central Arctic to multi-year observations within the Western Arctic (in Sec. 3.1); and second, the multi-year time series analysis of the MPC properties (Sec. 3.2). To account for this, the following discussion is split based on results reported in this study set into context with the MOSAiC expedition, and the results from the time series analysis.

On the MPC properties modulated as a function of SIC, coupling status, and pressure system

Section 3.1 along with Fig. 5 and Fig. 6 are only partially comparable to the findings reported by PSG23 for the MOSAiC expedition. ~~As previously mentioned, this~~ This is because the MOSAiC study mainly relies on the sea ice lead fraction (LF) to

represent the sea ice states. ~~Contrarily, for~~ For the present study, long-term and continues LF data are not available. Furthermore, SIC MOSAiC winter was mostly above 90%~~while~~ , in contrast to NSA site observations during the 14 years ~~of Nov-April observations at NSA site considered here, a large~~ where a larger variation in SIC was covered. Keeping these caveats in mind, the following phenomena reported by Saavedra Garfias et al. (2023) can be confirmed:

- LWP of coupled ~~wintertime MPC~~ clouds increases as the sea ice states trend to larger openings, whereas ~~decoupled LWP~~ LWP of decoupled clouds has no relationship with SIC. The present study ~~thus~~ confirms MOSAiC findings and extends its validity for SIC as low as 5%.
- Cloud layers for coupled cases are thicker and have a lower liquid layer base height than the decoupled cases.
- ~~The temperature lapse-rate within the cloud layer (Γ_{cloud}) for coupled cases and~~ For coupled cases with SIC>95%~~is distributed~~ , cloud layer temperature lapse-rate (Γ_{cloud}) ranges from negative to positive values~~while decoupled cases have~~ , whereas decoupled cases show a distribution predominantly above zero. For SIC<95%, Γ_{cloud} increases with increasing sea ice opening~~for both coupled and decoupled clouds~~, regardless of coupling status.

Conversely, new findings that the study from the MOSAiC expedition did not conclude ~~(e.g. because no distinction between pressure system was made there)~~ can be summarized as follows:

- ~~Coupled~~ Under L-pressure systems and for all SIC, coupled clouds have a lower liquid cloud base height ~~is lower than for the decoupled cases for L-pressure systems and all SIC. For H-pressure systems that~~ than decoupled clouds. This difference is only evident for H-pressure systems when SIC $\gtrsim$ 95%.
- A negative relationship between IWP and SIC was found, albeit only for coupled MPC.
- The liquid and ice effective radii (r_{eff}), which Saavedra Garfias et al. (2023) reported ~~not to present a~~ for MOSAiC showed no clear difference when sorted by ~~coupled~~ coupling status or lead fraction, ~~was found to have a strong dependency on SIC for~~ were found to exhibit a strong dependence on SIC in coupled cases. Specifically, r_{eff} ~~were found to increase~~ increased with decreasing SIC.
- For coupled MPC, a negative Γ_{cloud} (in-cloud temperature inversion) is possible at SIC>95%~~is possible. For low SICvalues the~~ . At lower SIC, $\Gamma_{\text{cloud}} > 0$ ~~, i.e. a tendency towards~~ shows a tendency toward a moist adiabatic lapse-rate~~is observed. Decoupled Γ_{cloud} cases exclusively show~~ . Decoupled cases consistently exhibit a moist adiabatic lapse-rate~~enhancing in~~ , with increasing magnitude as SIC ~~reduces, especially for~~ decreases particularly under L-pressure systems.

On the long-term trends of MPC properties

~~The application of two methods for trend estimation has shown a dependency of results based on the specific procedure adopted for trend estimation . Although method~~ Two trend estimation methods highlight method-dependent biases. Method ~~i~~is

~~a standard procedure for signals with stochastic variability or well-known periodicity, its biggest limitation is the sensitivity to the edges and the width of moving average window. That is especially the case for finite oscillatory signals, where the time series' cut-off edges produce the average window to be either overestimated (signal crest) or underestimated (signal trough). Disagreements in the method's results refer to the magnitude of the trends and the tendency of change. For instance, for L-pressure trends of LWP of decoupled MPC differ considerably from~~ , a standard approach for stochastic of periodic signals, is sensitive to edge effects and moving window width. Disagreements arise, particularly in L-pressure decoupled LWP trends: method *i* ~~(~~show a decline of -5.3±0.7 $\mathrm{g\,m^{-2}\,dec^{-1}}$~~) versus~~ , while method *ii* ~~(~~indicates a slight increase of +0.9±0.9 $\mathrm{g\,m^{-2}\,dec^{-1}}$~~). The underlying reason for that is that for all time-series method~~ . This discrepancy stems from Method *i*~~uses a constant moving~~ 's fixed window size, ~~whereas the best cyclical signal fit suggests a period of~~ which over-smooth the data, whereas method *ii* captures a dominant 6.5 years ~~which is much lower than the window size (~~cycle -shorter than the 10 years ~~), thus method *i* oversmooth the time series~~window- leading to more accurate trend representation.

~~An example of tendency disagreement~~ Disagreement also occurs for the liquid cloud base height of decoupled MPC~~, where method~~ . Method *i* ~~results in a positive~~ detects a trend of +54.9±1.0 $\mathrm{m\,dec^{-1}}$ ~~in contradiction to~~ , while method *ii* ~~with~~ reveals a negative trend of -228.1±1.5 $\mathrm{m\,dec^{-1}}$ ~~, both~~ both statistically significant. Figure 8 (c) shows how method *ii* ~~favours~~ captures a periodic signal of ~3.6 years~~to properly fit~~ , which better fits the low CBH values observed during negative ENSO phases (e.g. 2018/19, 2022/23), whereas method *i* ~~with an average window of ±5 yr smoothes out these low CBH observations~~effectively suppresses these short-term variations.

~~The IWP (shown in supplementary material S2.2) for H-pressureshows a remarkable agreement of both methods, with a trend for coupled cases~~ Both methods agree on IWP trends under H-pressure, showing coupled case trends of +3.5±0.8 $\mathrm{g\,m^{-2}\,dec^{-1}}$ (method *i*) and +4.4±1.0 $\mathrm{g\,m^{-2}\,dec^{-1}}$ ~~for method *i* and~~ (method *ii*~~, respectively, at a signal period of~~) with a 10.8 ~~years (~~year period characteristic for ENSO and PDO (supplementary material S2.2).

~~The assumption that climate modes variability might modulate the observed oscillatory nature of MPC properties has been tested by fitting~~ Hypothesizing the influence of climate models on MPC variability, we fit the data to Eq. 4b with one relevant harmonic as a free parameter ν_k. ~~In other words, the NSA site observations' time series can be explained by the ENSO, PDO, or AOcharacteristic intra-decadal periods. Among the values of ν_k, it has been found that the PDO and ENSO period of 10.8 or~~ The NSA site time series are best explained by ENSO's 5.4 ~~years are representative for the fluctuation of several MPC parameters. The ENSO and AO period of~~ and 10.8 years, PDO's 6.5 and 10.8 years, and AO's 2.3 and 2.9 ~~years are the second most frequent. AO and PDO 's period of~~ year periods. ENSO and PDO (10.8, 5.4 year) dominate most MPC parameters, with AO (2.3, 2.9 year) and PDO (6.5 ~~has additionally been found among the best fits. In summary, properties of decoupled~~ year) as secondary contributions. Decoupled MPC under H-pressure ~~influence vary within middle range~~ varies on intermediate periods (3.6, 4.0, 5.4 years), while coupled MPC ~~variation in on longer periods~~ shows longer cycles (6.5, 10.8 years). ~~Conversely, the variability of decoupled MPC L-pressure cases is mostly found~~ Under L-pressure, decoupled MPC oscillates at 2.3 to 6.5 years, ~~while properties of coupled MPC cases mostly oscillate~~ and coupled MPC at 2.9, and 10.8 years, depending on the specific MPC property.

Conclusions

The method proposed by Saavedra Garfias et al. (2023) to study the relationships of atmospheric boundary layer MPC properties coupled to sea ice leads during the MOSAiC expedition in the central Arctic has been successfully implemented and extended to the Western Arctic. Fourteen winter seasons of multi-sensor~~synergistic observations by~~ , synergistic observations from the ARM's NSA site were analysed alongside satellite-derived sea ice concentration to characterize MPC properties~~along with space-borne observed sea ice conditions. We found a remarkable relationship between the reduction of~~ . A remarkable relationship was found between decreasing sea ice concentration and ~~an increase of some MPC properties such as LWP, effective radius~~ increases in key MPC properties –LWP, effective radii of cloud droplets and ice particles~~effective~~, and cloud top temperature (CTT).

The MOSAiC ~~expedition's systematic difference between MPC properties belonging to clouds coupled or decoupled via the~~ 's derived distinction between coupled and decoupled MPCs, based on water vapour transport-sea ice ~~system has been confirmed for the NSA site. Additionally, the~~ interaction, is confirmed at the NSA site. The multi-year ~~dataset allowed to study~~ NSA dataset further enabled assessment of the influence of ~~the weather pressure system in which the observation took place. We found that some MPC properties can increase or decrease in magnitude depending~~ atmospheric pressure systems. Results show that MPC properties depend not only on ~~their~~ coupling status but also ~~as a function of the atmospheric~~ on the prevailing weather pressure system. ~~Conclusive is that for L-pressure systemsthe long-term rate of change for~~ Under L-pressure systems, coupled LWP, cloud top temperature, and liquid layer base height ~~in wintertime MPC is positive for coupled cases. For decoupled cases , no~~ exhibit positive long-term trends. In contrast, decoupled cases show no significant trend in LWP ~~and CTTwas detectable~~ or CTT, while liquid layer base height was found to decrease. ~~When H-pressure systemsare considered, mostly the same tendency of change in wintertime MPC properties was found albeit with different~~ Under H-pressure systems, similar directional trends are observed, albeit with differing magnitudes.

~~We applied two methods to estimate the rate of change of MPC properties and found that the method used plays a decisive role: the estimated time series trends were found to depend on which methods was applied. Furthermore, we discovered that Arctic wintertime MPC properties fluctuate over time analogous to oscillations of Arctic relevant climate modes, like ENSO, PDO, or AO. This commonality permits the exploitation of known ENSO or PDO frequencies of oscillation to physically constrain the detected undulating nature of MPC properties. Although trends are accurately estimated, the robustness of statistically significant trends will be strengthen as more years of observations will modify or confirm the significance of our results. We found that properties like LWP, CTT, and surface skin temperature show features that resemble ENSO cycles, with maxima/minima for years characterized by El Niño/La Niña events, respectively.~~ Based on time series of surface skin temperature as indicator of coupled clouds radiative feedback, we found that a continuing warming in the Western Arctic can only be ~~reckoned under a L-pressure system linked to observations with~~ attributed to L-pressure systems associated with observations under SIC<95%. ~~Contrarily~~In contrast, under high pressure systems and SIC≥95%, our results show ~~that the cloud radiative induced surface temperatureis decreasing~~a decrease in cloud radiative-induced surface temperature. A limitation of this study is that the current ~~NSA site~~ remote sensing capabilities ~~does~~ at the NSA site do not provide vertical ~~profile information about~~

aerosolsprofiles of aerosols, which hinders the study of the effects of aerosols to investigation of aerosol effects on LWP and IWP in conjunction to SIC changes.

This study put into consideration uses empirical mathematical models derived from long-term observations as parameterization for the modelling of to parameterize atmospheric boundary layer MPC ascribed to Arctic sea ice conditions. We suggest that the sea ice-atmospheric feedback processes that are represented in Arctic weather and climate models certainly should aim to mirror the complexity of relationships that the present study has uncovered. This implies the consideration of not only argue that Arctic climate models should capture the complexity revealed here –beyond small-scale horizontal moist air mass transport that serves as physical link between sea ice openings and clouds downstream , but also linking sea ice leads to downstream clouds– by incorporating weather patterns, large-scale atmospheric circulationprocessescirculation, intra- and multi-decadal climate oscillations, and teleconnections between the Arctic and lower latitudesArctic-lower latitude teleconnections. Recent studies reported that this complexity has implications for the prospect of highlight the implications of this complexity for decadal climate predictability (Timmermann et al., 2018; Mann et al., 2020; Cesana et al., 2025). Similar findings were recently , with similar findings reported by Lubin et al. (2026). They analysed , who linked long-term LWP and CRE trends from 1999 to 2024 and reported an influence by large scale (1999–2024) to large-scale circulation and atmospheric riversin long-term trends. With this study we acknowledge the immense importance of . Our findings are aligned to those studies and underscore the critical role of sustained Arctic monitoring at long-term stations like the ARM NSA site for the continuous monitoring of the Arctic which made this study possible. enabling such insights.

Code and data availability. Code and data available at Saavedra Garfias (2022) and references listed in Table 1.

Appendix A: Statistical parameters used in the data analysis

The statistics for cloud properties are represented by the geometric mean, median or 1st and 3rd quantile. The variability within the distribution is expressed by the standard deviation (σ_g) or MAD (σ_{mad}). When the data mean or median is used to fit an analytical model, the variability within the distribution is taken into account by performing a weighted fitting either by linear or non-linear regression. The weights are modelled as

$$\omega_j = \frac{\sigma_j^{-2}}{\langle \sigma_j^{-2} \rangle} \tag{A1}$$

with σ_j^{-2} is the inverse of the variance (with σ_j can be σ_g or σ_{mad}), and $\langle \sigma_j^{-2} \rangle = \frac{1}{N} \sum_j \sigma_j^{-2}$ is the inverse variance mean. The index j represents a distribution of cloud properties, which for the case of Sec. 3.1 $j \in SIC = \{10, 20, \ldots, 100\}$ is the distribution within binned sea ice concentration, and for the case of Sec. 3.2 $j \in WT = \{2011/12, \ldots, 2024/25\}$ for the wintertime. In both cases N is the length of j set. The Eq. A1 penalize large variability within the distribution j and will influence less the fitting algorithm.

A1 Model Goodness of fit test

To quantify the degree of a fitted model can represent the observations, the following parameters for goodness of fit are used:

- χ^2: is the sum over residuals square divided by the fitting model degrees of freedom ν, which indicates how close the model prediction is from the data,

$$\chi^2 = \frac{1}{\nu}\sum_{j=1}^{N}\left(\frac{\varepsilon_j}{\sigma_j}\right)^2 \tag{A2}$$

  where $\varepsilon = \hat{y_j} - y_j$ are the residuals (difference between model prediction $\hat{y_j}$ and observed value y_j) in Eq. 3, Eq. 4a, and Eq. 4b; with ν =2, 2, and 4, respectively. The closer χ^2 is to zero, the better the fir curve represent the data.

- r^2: is the coefficient of determination, which quantifies how good the model explains the change in observed value,

$$r^2 = 1 - \frac{\sum\limits_j \varepsilon_j^2}{\sum\limits_j (\langle y_j \rangle - y_j)^2} \tag{A3}$$

  where $\langle y_j \rangle$ is the average over all observed values y_j. Worth to note that r^2 is generally a valid parameter for linear relationships, while for non-linear regression it could produce unexpected results like negative values or larger than one (Spiess and Neumeyer, 2010).

- nRMSE: is the normalized root mean square error, which is the overall mean squared residual between model fitted and observed value,

$$\text{nRMSE} = \frac{\sqrt{\frac{1}{N}\sum\limits_j (\omega_j^2 \varepsilon_j^2)}}{\text{IQR}} \tag{A4}$$

  with IQR is the distribution inter-quantile region, and ω_j the weights as in Eq. A1. Values of nRMSE larger than one signalize a very poor agreement between fitted model and observations.

Given a set of fitted parameters to Eq.4b corresponding to the six ν_k values, a goodness of fit test is performed to determine which single ν_k represents the data the best. This is done by minimizing a cost function which is dependent of all three goodness of fit parameter χ^2, nRMSE, and the reciprocal of r^2 i.e. 1-r^2, thus all three parameters range from zero (best) to higher values (worst):

$$\mathcal{L} = \sqrt{\chi^2 + \text{nRMSE}^2 + (1 - r^2)} \tag{A5}$$

As an example of how the minimum is found, in Fig. A1 can be seen the cost function for two MPC parameters: LWP and CTT, with the minimum of the cost function $\mathcal{L}$ indicated by the vertical thick line.

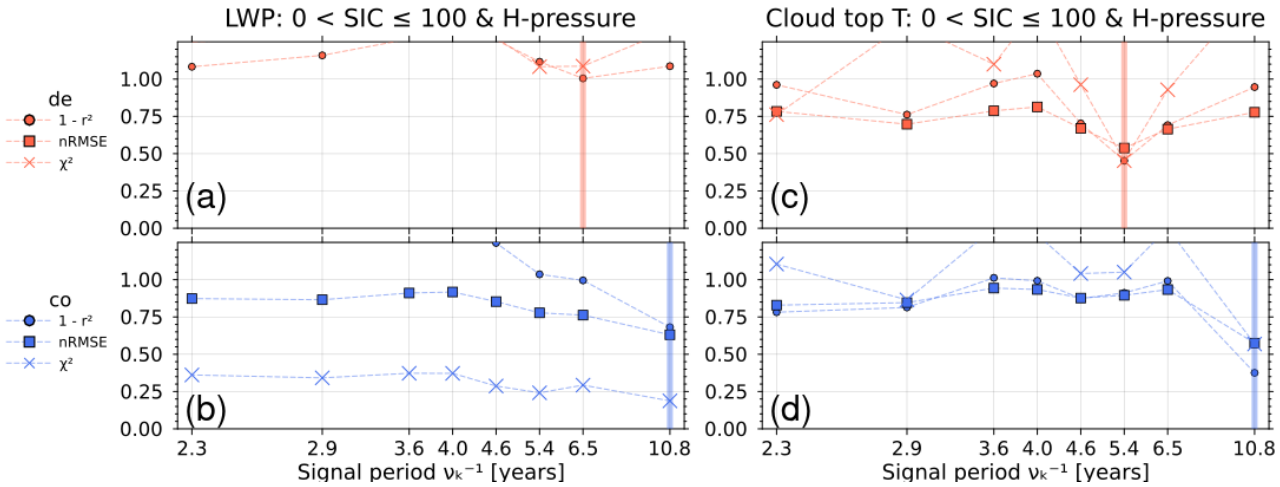


Figure A1. Determination of the best ν_k value, from the combination of all three goodness of fit parameters. LWP coupled (a) and decoupled (b), cloud top temperature coupled (c) and decoupled (d). The χ^2 is shown as crosses, nRMSE as squares, and the reciprocal of r^2 as circles. The thick vertical line is the value of ν_k that minimizes the cost function $\mathcal{L}$.

Appendix B: Results for trend estimation

To complement Sec. 3.2.2, the equivalent of Fig. 8 but for L-pressure systems is shown in Fig. B1 with LWP in panels (a) and (b), liquid CBH in panels (c) and (d), and cloud top temperature in panels (e) and (f). Further results of time series trends of other MPC properties can be found in the supplementary material.

B1 Time series for the lower/upper 50th percentile SIC decomposition

The time series' trend analysed by method *ii* are decomposed by the lower and upper 50th percentile of sea ice concentration. For the period of 14 years observations the lower 50th percentile comprises of data with SIC between 0% and 95%, whereas the upper half from SIC above 95% to 100%. Figure B2 shows the LWP SIC decomposition.

B2 Surface skin temperature trend results after SIC decomposition

Time series analysis for the surface skin temperature T_{skin}, estimated from the net down- and up-welling longwave radiation flux (Saavedra Garfias et al., 2024), or by down-welling infrared radiometer when the former data is not available, after being decomposed in SIC subsets of 50th percentiles (shown in Sec. S2.3, Fig. S8) applied to methods in Sec. 3.2.1 and Sec. 3.2.2 are displayed in Fig. B3. These results are discussed in Sec. 3 in relation to the warming in the western Arctic.

Appendix C: Sensitivity to radius of semi-circle around NSA site for SIC parameter

To investigate how sensitive the results are to the choice of sea ice area (red cone in Fig. 1) to compute the average SIC associated to be coupled/decoupled to the MPC parameters, in addition to the 50 km used for the results in Sec. 3, a different radius o´f 75 km has been tested. The procedure indicated in Sec. 2 was repeated for 75 km and the results for LWP trend are summarized in Table C1 as compared to the results for 50 km. It has been found that there is a small difference between results from 50 km and 75 km radius (second column in Table C1), but the differences are more noticeable for decoupled cases in particular when grouped to $0 \leq SIC < 95\%$.

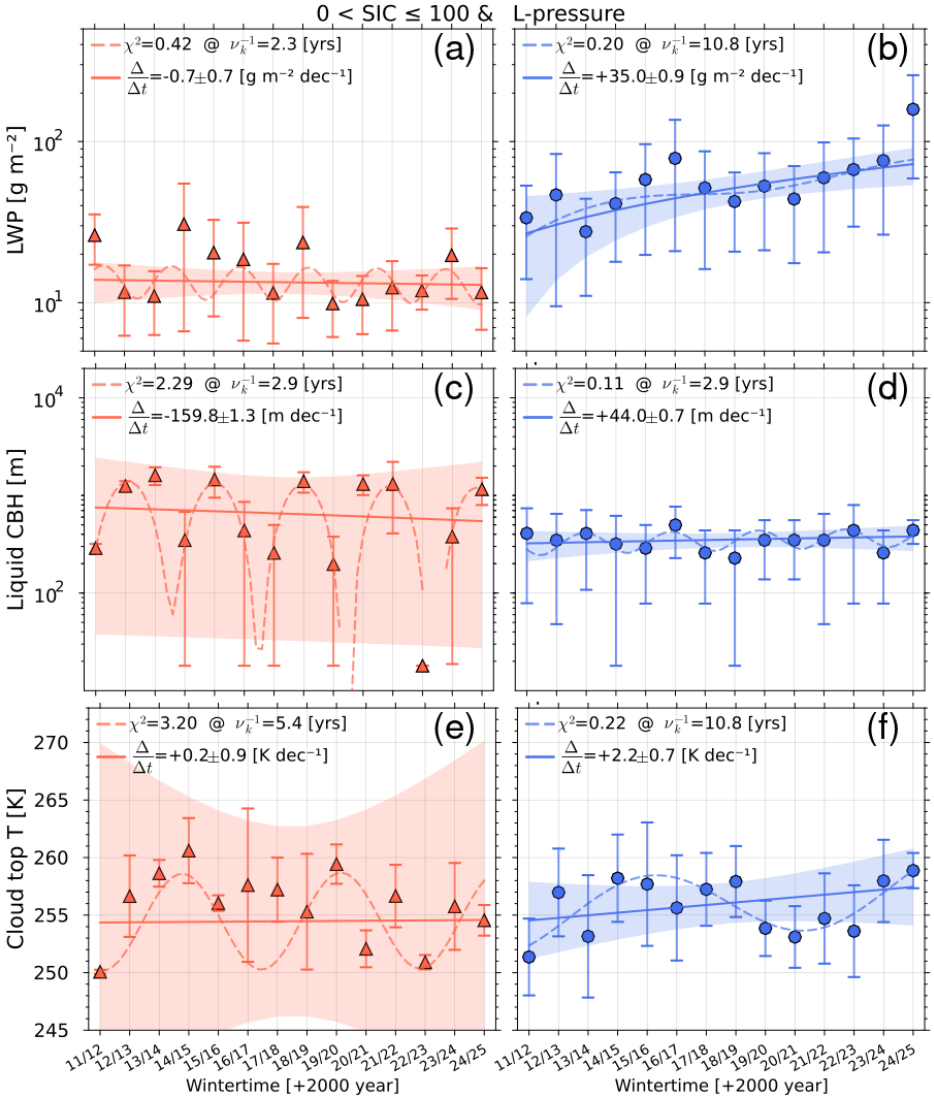


Figure B1. Same as in Sec. 3.2.2, Fig. 8 but for time series comprised of L-pressure systems.

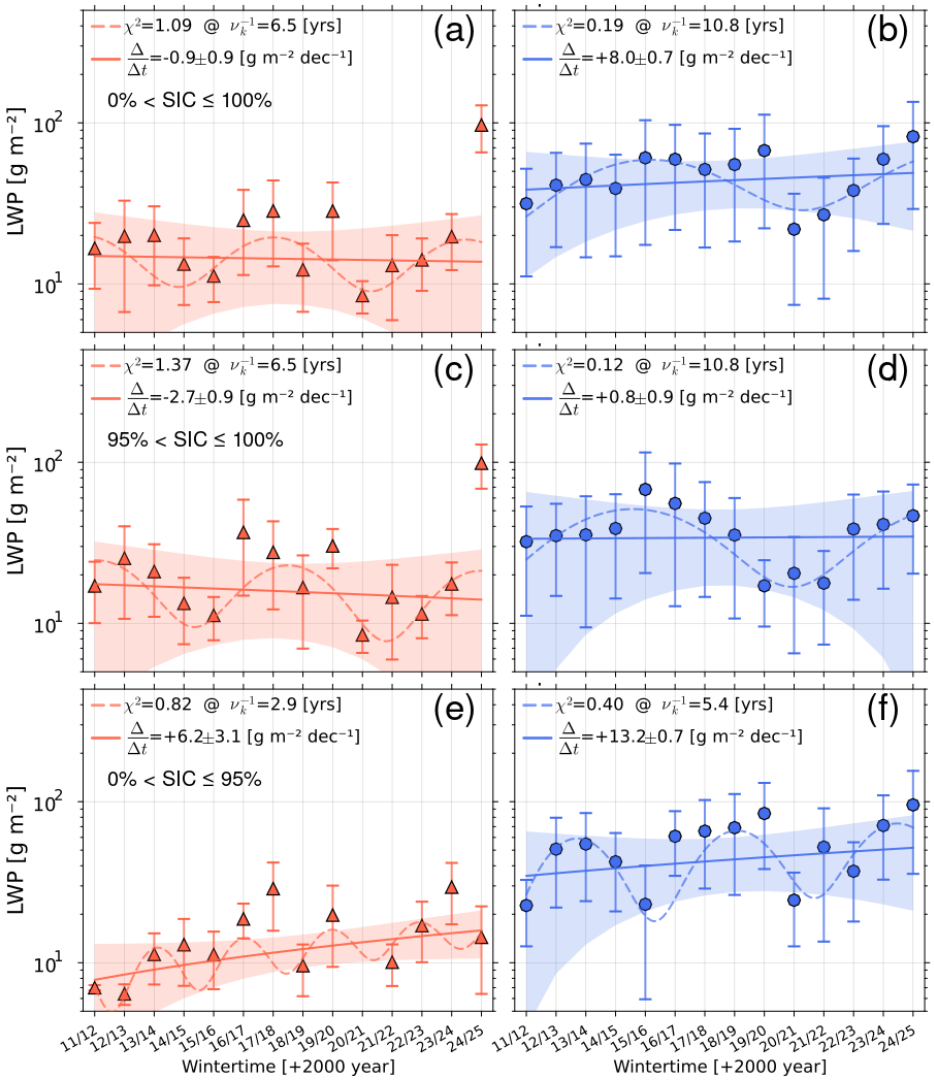


Figure B2. Time series of LWP for coupled and decoupled clouds under H-pressure systems. The time series are decomposed by the range of SIC: (a) and (b) all SIC considered, (c) and (d) for SIC > 95% and SIC $\leq$ 100%, and (e) and (f) for SIC > 0% and SIC $\leq$ 95%.

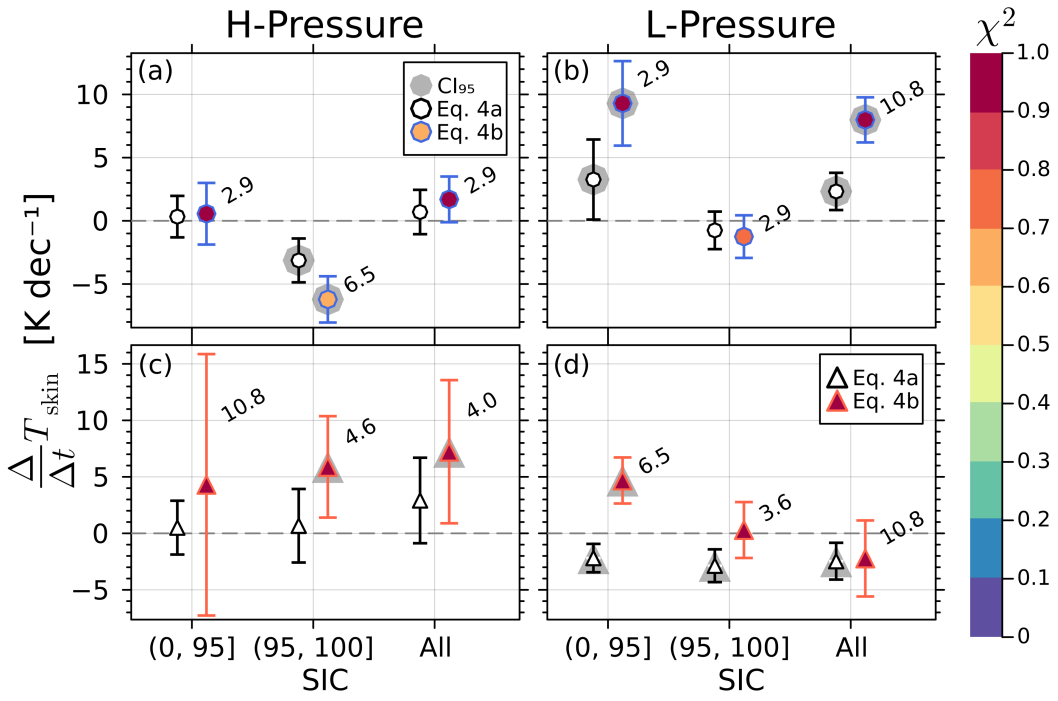


Figure B3. $T_{\rm skin}$ rate of change for SIC subsets in the abscissae. The hollow symbols are trends using method *i* (Eq. 4a), coloured symbols use method *ii* (Eq. 4b), grey shadows behind symbols indicate the trend is statistically significant (p<0.05), and the number next to the coloured symbols is the period in years for the best fit Eq. 4b. The colour table represents the goodness of fit χ^2 value. H-pressure systems in panel (a) and (c) for coupled and decoupled cases. L-pressure systems in panels (b) and (d) for coupled and decoupled, respectively.

In supplementary material (Sec. S3) the associated Figure for 75 km radius around NSA site can be found. A noticeable difference is mostly seen for the results associated to decoupled cases and SIC between 0 and 95%. For coupled cases the results are robust and consistent either by selecting SIC within 50 or 75 km.

Appendix D: Frequency decomposition for climate indicators

A discrete Fourier analysis has been performed to obtain the frequency harmonics ν_k from three climate indicators: Arctic oscillation (AO), Pacific Decadal Oscillation (PDO), and El Niño Southern Oscillation (ENSO). The power spectrum as a function of the signal harmonics expressed as periods (ν_k^{-1}) is shown in Fig. D1, with the set of harmonics used to test the fitting of Eq. 4b indicated by a red triangle at the bottom of panel (c) in Fig. D1. Note that the limits of the abscess in Fig. D1 is intentionally cut for the range relevant to the 12 year of observation period, the signal can contain multi-decadal harmonics that excesses the 12 years period.

Table C1. Comparison for 2011 to 2024 wintertime LWP trends when considering SIC within two sectors of radius 50 km or 75 km.

High Pressure systems ($\Delta Z < 0$)								
SIC	R_{sic}	Decoupled			Coupled			Reference
[%]	[km]	χ^2	ν_k^{-1} [yrs]	$\frac{\Delta}{\Delta t}$LWP [$g\,m^{-2}\,dec^{-1}$]	χ^2	ν_k^{-1} [yrs]	$\frac{\Delta}{\Delta t}$LWP [$g\,m^{-2}\,dec^{-1}$]	figure
0–100	50	1.09	6.5	-0.9 $\pm$ 0.9	0.19	10.8	+8.0 $\pm$ 0.7	8 (a, b)
	75	1.26	2.3	-3.2 $\pm$ 1.3	0.17	10.8	+10.2 $\pm$ 0.7	S13 (a, b)
95–100	50	1.37	6.5	-2.7 $\pm$ 0.9	0.12	10.8	+0.8 $\pm$ 0.9	B2 (c, d)
	75	1.44	6.5	-6.9 $\pm$ 1.2	0.15	10.8	+0.1 $\pm$ 0.8	S13 (c, d)
0–95	50	0.82	2.9	+6.2 $\pm$ 3.1	0.40	5.4	+13.2 $\pm$ 0.7	B2 (e, f)
	75	1.30	2.3	-24.0 $\pm$ 1.2	0.39	2.3	+21.8 $\pm$ 1.0	S13 (e, f)
Low Pressure systems ($\Delta Z > 0$)								
SIC	R_{sic}	Decoupled			Coupled			Reference
[%]	[km]	χ^2	ν_k^{-1} [yrs]	$\frac{\Delta}{\Delta t}$LWP [$g\,m^{-2}\,dec^{-1}$]	χ^2	ν_k^{-1} [yrs]	$\frac{\Delta}{\Delta t}$LWP [$g\,m^{-2}\,dec^{-1}$]	figure
0–100	50	0.42	2.3	-0.7 $\pm$ 0.7	0.20	10.8	+35.0 $\pm$ 0.9	S8 (a,b)
	75	0.49	3.6	+0.3 $\pm$ 0.7	0.21	10.8	+34.3 $\pm$ 0.9	S12 (a, b)
95–100	50	0.94	2.3	-0.3 $\pm$ 0.7	0.13	2.9	+15.3 $\pm$ 0.8	S8 (c,d)
	75	1.35	2.9	+1.3 $\pm$ 0.6	0.11	2.9	+17.6 $\pm$ 0.7	S12 (c, d)
0–95	50	1.37	4.0	-5.4 $\pm$ 1.3	0.64	4.6	+86.8 $\pm$ 3.7	S8 (e,f)
	75	1.13	2.9	+3.3 $\pm$ 17.9	0.32	4.6	+79.9 $\pm$ 0.8	S12 (e, f)

Appendix E: List of Acronyms and variables

Acronym	Description
AMSR2	Advanced Microwave Scanning Radiometer 2
AO	Arctic Oscillation
ASI	Arctic sea ice algorithm
CEIL10m	Ceilometer 10 m resolution
CRE	Cloud Radiative Effect
ENSO	El Niño Southern Oscillation
INTERPSONDE	Interpolated Radiosonde
KAZR	Ka Zenith Radar
MPC	Mixed-phase Clouds
NSA	North Slope of Alaska
MWR	Microwave Radiometer
PDO	Pacific Decadal Oscillation

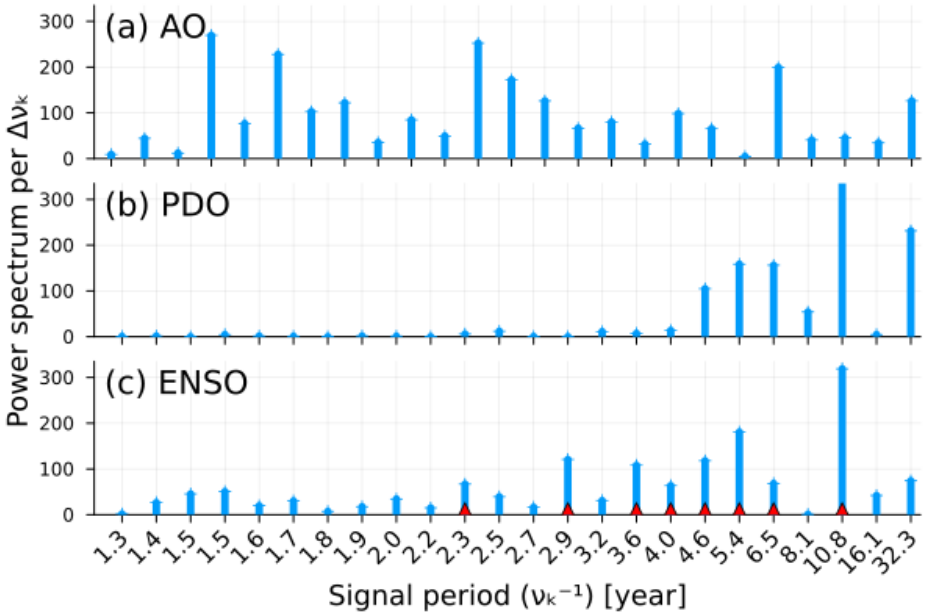


Figure D1. Power spectrum per frequency bandwidth for three climate indicators: (a) Arctic Oscillation, (b) Pacific Decadal Oscillation, (c) El Niño Southern Oscillation. The relevant frequencies are indicated by red triangles at the bottom of panel (c). Note, the peak at 10.5 year in panel (b) is cut at 300 for comparison reasons.

Symbol	Description	Unit
LWP	liquid water path	$\mathrm{g\ m^{-2}}$
IWP	ice water path	$\mathrm{g\ m^{-2}}$
∇_zWVT	vertical gradient of water vapour transport	$\mathrm{kg\ m^{-2}\ s^{-1}}$
CBH	liquid cloud base height	m
CTH	cloud top height	m
CMLH	cloud mixing-layer height	m
CTT	cloud top temperature	K
SIC	sea ice concentration	%
Ze	radar equivalent reflectivity factor	dBz
β	lidar attenuated backscattering coefficient	$\mathrm{m^{-1}\ sr^{-1}}$
P	atmospheric pressure	Pa
q_v	specific humidity	$\mathrm{g\ g^{-1}}$
$\boldsymbol{v}_w$	horizontal wind speed	$\mathrm{m\ s^{-1}}$
W_d	wind direction from North	°
θ_v	virtual potential temperature	K
Ri_b	bulk Richardson number	-
T_{skin}	skin surface temperature	K
Γ_{cloud}	cloud layer temperature lapse rate	$\mathrm{K\ km^{-1}}$
r_{eff}	cloud layer average effective radius	μm

Author contributions. PSG conceptualized the research idea, performed the data processing, and analysis of results. HKL conceptualized the research idea, provided advise and supervision. Both authors were involved in the manuscript preparation.

Competing interests. No competing interests.

Acknowledgements. Our gratitude to the DOE ARM program for openly provide the data from its North Slope of Alaska site in Utqiagvik Alaska, and to the open Sea Ice data repository from the University of Bremen. We gratefully acknowledge the funding by the Deutsche Forschungsgemeinschaft (DFG, German Research Foundation) - Projektnummer 268020496 - TRR 172, within the Transregional Collaborative Research Center "ArctiC Amplification: Climate Relevant Atmospheric and SurfaCe Processes, and Feedback Mechanisms (AC)3". This work was funded by the Open Access Publishing Fund of Leipzig University supported by the DFG within the program Open Access Publication Funding. We acknowledge ACTRIS and Finnish Meteorological Institute for providing the data set which is available for download from https://cloudnet.fmi.fi. We acknowledge ECMWF for providing IFS model data.